DENG, WENSHENG, Ph.D., April, 2002 PHYSICS

CHARGED KAON PRODUCTION IN AU+AU COLLISIONS AT $\sqrt{S_{NN}} = 130$ GEV (81 pp.)

Director of Dissertation: Spyridon Margetis

We studied the kaon production in Au+Au collisions at $\sqrt{s_{NN}} = 130$ GeV. We obtained a K^+/K^- ratio of 1.14 ± 0.01 at mid-rapidity for central collisions. The ratio indicates that the mid-rapidity region is almost (but not completely) net-baryon free. This K^+/K^- ratio value can be simply related to (or even be predicted by) other measured particle/anti–particle ratios in the framework of a simple quark-counting model. Our measurement is compatible and in good agreement with the other measurements performed in the same experiment. The observed trend in these particle ratios is similar to that observed in heavy-ion collisions at the lower CERN-SPS energies.

We also report first measurement of the transverse mass spectra and mid-rapidity yields of charged kaons in these collisions. The spectra are well described by an exponential in transverse mass, with a slope parameter of about 280 MeV for central collisions, showing slight increase with the collision centrality. For central collisions, the mid-rapidity yields are about 48 for K^+, 42 for K^-, and the negative kaon to pion ratio is $0.15 \pm 0.01(stat) \pm 0.02(sys)$. No strong centrality dependence is found for the kaon to pion ratios. The K/π ratios are found to be enhanced by about 50% from similar energy $p+p$ and $\bar{p}+p$ collisions. The negative kaon to pion ratio is found, as a function of the pion transverse energy density, to increase as a function of the colliding energy, and seems to saturate at the RHIC energy.

CHARGED KAON PRODUCTION IN AU+AU COLLISIONS AT $\sqrt{S_{NN}} = 130$ GEV

A dissertation submitted to
Kent State University in partial
fulfillment of the requirements for the
degree of Doctor of Philosophy

by

Wensheng Deng

April, 2002

Dissertation written by

Wensheng Deng

B.S., Wuhan University, 1989

M.S., Nankai University, 1992

Ph.D., Kent State University, 2002

Approved by

_____ , Chair, Doctoral Dissertation Committee

_____ , Members, Doctoral Dissertation Committee

_____ ,

_____ ,

_____ ,

Accepted by

_____ , Chair, Department of Physics

_____ , Dean, College of Arts and Sciences

TABLE OF CONTENTS

LIST OF FIGURES

LIST OF TABLES

ACKNOWLEDGMENTS

First of all my gratitude goes to my advisor, Dr Spyridon Margetis, for bringing me to this wonderful field. Throughout my four-year graduate research in his group, he has not only given me tremendous precious advice which is essential to this thesis, but also shown great patience to endure my dullness and my English. The experience with him is unforgettable in my life.

Thanks to the professors and staff of the Physics department in Kent State University, their instruction and work are indispensable to my graduate research. Special thanks should go to the committee members of this thesis for their valuable comments.

Many thanks to Dr Fuqiang Wang for the valuable discussions with him. I am happy to extend my thanks to people who built the STAR experiment; hardware, software and management. Without their efforts, this thesis would not be possible. Thanks to the members of STAR computing group, I learn a lot from them.

Thanks to all of my classmates, especially Aihong Tang, for the joyful time I had with them. Thanks to Dr Lee Barnby, my officemate, for many valuable discussions.

Finally and most importantly I would like to express my heartfelt thanks to my wife, Danfeng Chen, for her love, sacrifice and patience. Without her encouragement, I would not have been able to complete this thesis work. Thanks also goes to my three year old son, Ran, for his support and the joy which he emits. Someday he will understand what I mean here.

CHAPTER 1

INTRODUCTION

Ultra-relativistic heavy-ion collisions provide an indispensable laboratory for investigating the behavior of nuclear matter under extreme conditions of temperature and/or pressure [1, 2]. In these collisions very hot and dense nuclear matter is produced having an estimated temperature of about a trillion degrees (10^{12}), and density several times higher than that of normal nuclear matter. Under these conditions, Lattice Quantum Chromo-Dynamics (QCD) calculations, as well as phenomenological models predict that a phase transition should occur to "deconfinement", a state in which partons (quarks and gluons) are no longer bound in individual hadrons but instead can freely move inside the whole interaction region. Such a state is usually referred to as Quark–Gluon Plasma (QGP). The experimental observation of this phase transition, and the study of the dynamics of this new phase of matter, would have important consequences, both for the understanding of QCD (in particular "non-perturbative" QCD), and also for cosmology, as a QGP recreates conditions which existed in the Universe as a whole some 10 μs after the Big Bang.

The recent assessment [3] of the results from the CERN-SPS heavy ion program [4] showed that deconfined matter might have been produced in central Pb–Pb collisions at incident energies of 158 GeV per nucleon fixed target (corresponding to $\sqrt{s_{NN}} = 17$ GeV. We use $\sqrt{s_{NN}}$ to denote the center-of-mass energy per nucleon pair). The verification of this statement and the study of the properties of this possible new phase of nuclear matter is now resting with RHIC, the Relativistic Heavy Ion Collider at Brookhaven National Laboratory.

Our study is part of an important measurement, that of strange particle production.

These measurements have consistently played an important role in revealing the production mechanisms in relativistic heavy ion collisions [5, 6, 7, 8, 9, 10]. In this dissertation, we will first introduce the physical arguments for performing such strangeness production measurements as a possible probe for deconfined matter. The specific experimental method used to extract strange particle signals in these very complicated collisions will be then described, and the obtained results presented. These results are discussed and compared to measurements, either in the same experiment, or in other experiments performed at lower energies or data from elementary nucleon–nucleon collisions.

1.1 PHYSICS MOTIVATION

1.1.1 Collisions of Heavy Ions

Figure 1 shows a near head-on collision between two heavy ions of equal mass. On the left side is shown a top view of the collision and on the right side the corresponding diagram in Minkowski's space. Initially the two nuclei approach each other with velocities near the speed of light, looking like two pancakes due to relativistic (Lorentz)contraction. Then, there is a collision phase where collisions among partons (mostly gluons) take place leading to a quick thermalization and (possibly) the creation of QGP. This phase is followed by a violent expansion, both in the longitudinal and the transverse directions which ends with the so called "chemical freezout", the point in time when all inelastic collisions among produced particles stop. The particle composition and yields are frozen at this point. In the next phase, only elastic collisions continue due to larger cross section ($\sigma_{el} > \sigma_{inel}$) and when they also cease to exist we have the "thermal freezout" when the momentum spectra of the produced particles are no longer changing (in other words, the particle mean free path is larger that the radius of the fireball, or equivalently, the particle density is very low). The emerging particles travel to the detectors of the experiment practically unaffected. The effort of the experimentalists is to search in the remnants of these violent collisions for

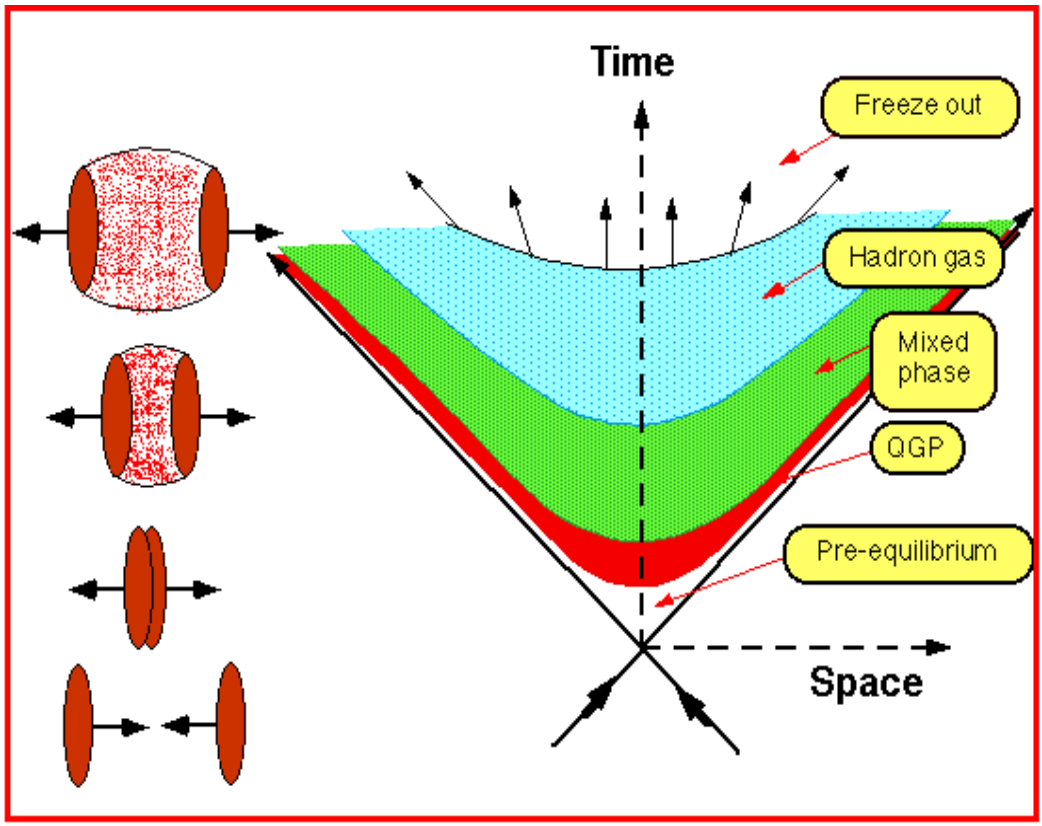

Figure 1: The space-time picture of an ultra-relativistic heavy-ion collision

signals, "signatures", of QGP creation.

Several different such signatures have been proposed for the observation of a QGP phase. Here we concentrate on the "strangeness enhancement", originally proposed by Rafelski, Hagedorn & Müller [11, 12, 13, 14]. This refers to an "enhanced" yield of strange particles produced in nuclear interactions relative to the elementary nucleon-nucleon ones, after trivial scaling effects (like volume) are taken out. This is a typical example of a hadronic probe. Its disadvantage, as with all hadronic probes, is that the hadrons undergo a substantial evolution through strong re-interactions in the period between when they are formed and when they are detected. The QGP has first to hadronize into resonances and particles, which then for some time will interact among themselves, both elastically and

inelastically, until their spatial density decreases sufficiently and the final hadrons freeze out. Therefore, both the momentum distributions and the final particle composition can be affected by later stages in the heavy-ion collision. We will argue, however, that despite this, we are able to access the properties of the first, very dense, stage of the collision by observing the strange, and especially multi-strange hadrons. By 'observing' we mean the measurement of the yields and spectra of the produced strange particles.

1.1.2 Strangeness and QGP

There are two reasons why strangeness production should be enhanced in a QGP scenario; the first is due to the large temperature expected to be achieved in the heavy-ion collision at high energies, and the second is an additional enhancement at large baryon densities. We discuss them in more detail below.

The QCD Lagrangian has an approximate symmetry; in the limit of vanishing quark masses ($m_{\mathrm{q}} \to 0$, where m_{q} are the quark masses entering the Lagrangian, i.e. the so-called "bare" or "current" masses) it reveals chiral symmetry. This is a flavor symmetry separately for left- and right-handed quarks with symmetry group $\mathrm{SU(3)_L} \times \mathrm{SU(3)_R}$ (where we neglect the masses of the three lightest quarks; u, d and s). The physical reason for chiral symmetry is that in this limit, the helicity becomes a "good" quantum number; massless quarks move in any system with the speed of light and therefore their helicity is invariant. Because the gluon field is a vector field, in this limit a left-handed quark interacts only with a left-handed antiquark and a right-handed quark interacts only with right-handed antiquarks. In addition, gluon interactions are completely democratic with respect to quark flavor, i.e. the couplings for gluon splitting into u, d or s quark–antiquark pairs are equal.

At zero and at low temperatures, chiral symmetry is dynamically broken, in addition to the explicit breaking due to the mass term in the Lagrangian. The reason for this is the existence of a quark condensate in the QCD vacuum at low temperatures. The following

argument is due to Gottfried & Weisskopf [15]. If we want to create a pair of color charges in a QCD vacuum at some distance r, these have to have a relative momentum of the order of $1/r$, as a consequence of uncertainty relation. At small distances (< 1 fm), the potential energy between the color charges will be of the order of $-4\pi\alpha_{\rm s}/r$. When the distance r increases from zero, the strong coupling $\alpha_{\rm s}$ also rises, starting from zero. Already at small distances, $\alpha_{\rm s}$ becomes large enough for the potential energy to overcome the kinetic energy $1/r$ (i.e. $1 < 4\pi\alpha_{\rm s}$), and the total energy of the color pair becomes negative. At larger distances the potential energy itself becomes positive and the total energy of the pair increases with the distance r. Therefore, at some distance ($r \sim 1$ fm), the total pair energy must have a minimum with a negative value. As a consequence the empty QCD vacuum is unstable; the vacuum is spontaneously filled by pairs of color charges (gg and $\rm q\overline{q}$) in singlet states at distances of the order of ~ 1 fm. If we now put into such a vacuum a test probe (see Müller [16]), e.g. a left-handed, massless quark, it can annihilate with a left-handed antiquark from the vacuum condensate. However, this left-handed antiquark has to have a nearby right-handed quark (as they have to compose spin singlets) which will be liberated in this way. For the outside observer it appears that our test quark spontaneously changed its helicity and therefore cannot be moving with the speed of light. Hence the test quark has to acquire a dynamical mass, sometimes called a constituent mass, $M_{\rm q} \approx M_{\rm B}/3 (\approx M_\rho/2) \approx 350$ MeV.

When we raise the temperature, we increase the kinetic energy of the vacuum color pairs. Above some critical value $T_{\rm c}$, the potential energy will no longer be able to compensate for this increase for any distance r. The energy of color pair will be always positive and the $\rm q\overline{q}$ condensate will disappear from the vacuum. As a consequence chiral symmetry will be restored (approximately, since the explicit breaking due to the mass term will remain) and the effective quark masses will drop from their dynamical values $M_{\rm q}$ to their bare values $m_{\rm q}$. This will happen at a critical temperature $T_{\rm c}$ as a phase transition, and the order

parameter of this phase transition is the vacuum expectation value of the $q\overline{q}$ condensate. The order of this phase transition, and the question whether it appears together with the other predicted phase transition, from a confined to a deconfined state, is the subject of extensive theoretical and experimental study, which is, however, beyond the scope of this dissertation.

At low temperatures strange quark production is suppressed due to its large dynamical mass $M_{\rm s} \approx 500$ MeV. The suppression factor with respect to u and d quark production (with dynamical masses $M_{\rm u,d} = M_{\rm q} \approx 350$ MeV), can be approximated by $\beta_{\rm s} \approx \exp\left[-(M_{\rm s}^2 + T^2)^{1/2}/T\right] / \exp\left[-(M_{\rm q}^2 + T^2)^{1/2}/T\right)$, which gives at typical hadronic temperature $T = 150$ MeV the value $\beta_{\rm s} \approx 0.4$. Note that the more usual strangeness suppression factor $\lambda_{\rm s}$, introduced by Wróblewski [17], includes the effect of dilution from resonance decays, and is typically a factor 2 lower than $\beta_{\rm s}$. Thus the experimentally observed ratio in elementary nucleon-nucleon collisions is $\lambda_{\rm s} = 0.2$.

Now if we assume chiral symmetry restoration, the masses will suddenly drop, so we have to substitute the dynamical masses with bare masses $M_{\rm s} \to m_{\rm s} \approx 150$ MeV and $M_{\rm q} \to m_{\rm q} \approx 0$ MeV. For the same temperature $T = 150$ MeV, $\beta_{\rm s}$ increases to about 0.7, i.e. by a factor 2. Therefore, as a consequence of the chiral symmetry restoration, we would observe a global strangeness enhancement by a factor of about 2.

A second reason for a strangeness enhancement (which is more relevant at the BNL–AGS and CERN–SPS energies) arises when there is large baryon stopping. Central nuclear collisions at these lower energies have a large baryon number density even at mid-rapidity, which corresponds to a baryonic chemical potential $\mu_{\rm B} \approx 200$–250 MeV. Therefore, if the hadronic matter is deconfined during the collision, the production of u and d quarks will be suppressed due to Pauli blocking [18], i.e. the fireball volume is already occupied by many u and d quarks coming from the interacting nuclei and as a consequence the production of non-strange quarks is suppressed. We would therefore expect an even stronger increase of

strangeness production in such baryon dense scenario.

Furthermore, the strangeness enhancement will be more pronounced for particles which contain more than one strange quark, i.e. the ϕ meson and the cascade baryons (Ξ^- and Ω^-). In a first approximation, if they are produced by a recombination of quarks from a QGP, we would expect that ϕ and Ξ^- production will be enhanced by a factor of more than $2^2 = 4$ and the Ω^- production by a factor of more than $2.^3 \approx 8$. These estimates, however, do not take into account many important details, such as the actual hadronization process and hadron wave functions.

Strangeness production can also be enhanced in a "normal hadronic" scenario. If, during the heavy-ion collision, the gas of produced hadrons has enough time to interact, the inelastic collisions will drive the system towards chemical equilibrium. In this scenario, at the beginning strangeness production is suppressed and during the hadronic re-interactions the strangeness content will increase with time. A typical inelastic process of this type is $\pi^0 + \mathrm{p} \rightarrow \mathrm{K}^+ + \Lambda$. Once we produce a strange particle, the probability to destroy it is very low, because it interacts mostly with pions and nucleons (until the strangeness density increases to its equilibrium value). For multi-strange hadrons hadronic re-interactions will be much less effective, i.e. it is much harder in a hadronic scenario to produce multi-strange particles. In order to produce, for example, an Ω^- we have to go through the following reaction chain: (*i*) $\pi^0 + \mathrm{p} \rightarrow \mathrm{K}^+ + \Lambda$, (*ii*) $\pi^0 + \Lambda \rightarrow \mathrm{K}^+ + \Xi^-$, (*iii*) $\pi^+ + \Xi^- \rightarrow \mathrm{K}^+ + \Omega^-$. This chain has a low probability and therefore needs a long time. In addition, multi-strange particles can easily be destroyed in subsequent interactions with pions or nucleons, giving rise to singly strange particles in the final state. Therefore, the approach to chemical equilibrium for the Ω^- by such a cascade mechanism will be very slow. For the $\overline{\Omega}^+$ we would have to go through another small cross-section process, the production of an antibaryon, which will further increase the equilibration time. The direct production of an Ω^- $\overline{\Omega}^+$ pair is strongly suppressed because of the high threshold (above 3 GeV for $\pi^+\pi^-$ annihilation).

Estimates show [19, 20], that the chemical equilibration time in a hadronic gas for $\overline{\Omega}^+$ will be of the order of 100 fm/c, while the typical timescale for a Pb–Pb collision is given by the size of the Pb nucleus and is only of the order of a few fm/c. On the other hand, in a QGP strangeness equilibration will proceed very fast, because of the gluon flavor democracy mentioned above. Once sufficient strangeness density is built up during the QGP phase, it is easy to fill the phase-space during hadronization according to the maximum entropy principle, i.e. according to chemical equilibrium. If the system later spends a significant time in the interacting hadronic phase, the temperature will decrease, which, if anything, will lower the chemical equilibrium yields of heavy particles like Ω^- and $\overline{\Omega}^+$. Therefore, the observation of an order of magnitude enhancement of multi-strange baryon production would be a strong argument in favor of the creation of a new state of matter during heavy-ion collisions.

1.1.3 Modeling Nuclear Collisions

Statistical Models

The use of thermal models to describe the hadron abundances in a heavy ion collision has been advocated ever since strangeness was originally proposed as a QGP probe [11, 13]. The models require the assumption that the particles achieve local thermal and chemical equilibrium. In practice, the system will evolve as it expands and cools before finally freezing out as cold non-interacting hadronic matter. Strictly, what is measured in heavy-ion collisions is the set of abundances in the final stage, when hadronic final-state interactions cease. However, as argued in the previous section and below, the flavor composition of the system should not change much through hadronic final-state interactions, and therefore the measured yields reflect the system at hadronization.

In this way, the equilibrium abundances for different particle species (when these have u, d and s quarks only as valence quarks) can be predicted in terms of just three numbers:

(*i*) the baryo-chemical potential $\mu_{\rm B}$, (*ii*) the strange chemical potential $\mu_{\rm s}$ and (*iii*) the temperature T. These determine the partition function $\mathcal{Z}$, and the hadron abundances are then given by

$$N_j = \lambda_j \frac{\partial}{\partial \lambda_j} \ln \mathcal{Z}(\mathcal{T}, \mathcal{V}, \ldots) \ , \tag{1.1}$$

where λ_j is the fugacity $\exp(-\mu_j/T)$ for particle j, and $\mu_j = n_j^{\rm q}\mu_{\rm q} + n_j^{\rm s}\mu_{\rm s}$, where $n_j^{\rm q}$ and $n_j^{\rm s}$ are the numbers of non-strange and strange valence quarks respectively for species j, and $\mu_{\rm q} = \mu_{\rm B}/3$.

In the processes studied to date, strangeness usually does not reach its full saturation value. In order to describe this, Rafelski [21] has proposed the use of a strangeness saturation factor $\gamma_{\rm s}$, which modifies the yields. In this description the yield for a particle with strangeness content $n_j^{\rm s}$ is reduced by the corresponding power of $\gamma_{\rm s}$, where $0 \leq \gamma_{\rm s} \leq 1$. The value of $\gamma_{\rm s}$ is particularly sensitive to multi-strange baryon yields, which are therefore a good indicator of strangeness saturation.

In order to obtain realistic values for strangeness yields, contributions from resonances must be taken into account. The yields for resonances can be determined according to the partition function Eq. 1.1, and their decays then give the contributions to the overall yield for "stable" strange particles. This could cause a problem, as the branching ratios for higher resonances are poorly known. Fortunately, the yields drop rapidly with increasing mass, and so a cut-off can be implemented above which resonance contributions may be safely neglected. Typically, this is set in the range 1.5–2.0 GeV.

Other corrections have been applied to take into account the finite size of the systems, which are among the smallest for which a thermal description can be used. For example, bearing in mind that the system is still very dense at chemical freeze-out, several models use an "excluded-volume" correction, in which hadrons are treated as finite size particles, which has the effect of reducing particle yields (though without changing ratios as it applies

to all particles equally). A discussion of this and other corrections is given by Sollfrank in [22].

It has been found that elementary collisions (e^+e^-, pp, and $\overline{p}p$ collisions) also exhibit "thermal" behavior, in the sense that here too the abundances of hadron species can be described in the framework of "temperatures" and "fugacities". In order to treat the relatively low multiplicities, a canonical approach is employed rather than the grand canonical approach described above. A detailed description of this formalism is given by Becattini & Heinz [23, 24], and the two descriptions are compared in Ref. [22]. What emerges is that here too particle yields are consistent with a freeze–out temperature of about 170 MeV, and a strangeness suppression factor $\beta_s \sim 0.4 - 0.5$. This happens despite the fact that in these collisions there is essentially no rescattering nor any final state interactions. It reflects the important fact that in these interactions particles are formed according to the maximum entropy principle, that is that the hadronization yields are the most probable ones.

The mechanism for hadron production in heavy-ion collisions is quite different. Here, a strongly interacting system persists for some considerable time, there are many collisions, and it is these which provide the means for equilibrium to be achieved. In particular, thermal equilibrium is driven by the total cross-section, while chemical (flavor) equilibrium is driven by the inelastic cross-section. As discussed in the previous section, the approach to flavor equilibrium is fast in a QGP, but slow in a hadronic phase. For this reason, hadron yields reflect conditions at hadronization.

The thermal behavior resulting from this mechanism has two distinguishing features. The first is enhanced strangeness production, especially for multi-strange particles, as discussed above. The second is the development of collective flow, which arises naturally from the many collisions in a heavy-ion interaction but which is not present in elementary processes. Both these features will be explored in detail in the remainder of this dissertation.

Microscopic Models

Initially, microscopic models were intended to describe nucleus-nucleus collisions based on a superposition of elementary hadronic interactions, and thus provide a "baseline", i.e. a description of what we would expect in a hadronic system without a QGP. The microscopic models, by taking out trivial effects such as the impact parameter dependence of an observable, and by describing the ordinary physics of nucleon-nucleon or nucleon-nucleus collisions, could allow us to recognize any emerging new physics in nucleus-nucleus collisions.

Depending on the version, almost every model evolved from independent, incoherent collisions between the interaction elements (hadrons or partons), to include the effects of rescattering and coherence such as string fusion, color ropes, quark droplets and interacting baryon junctions [25, 26, 27]. By "independence" we mean that the successive collisions of a projectile nucleon with the target nucleons do not influence each other. and by "incoherence" that adjacent nucleons in the projectile do not influence each others' interactions with the target nucleons. In practice, more and more "collective" or "nuclear" features have been added to these models, in order to describe the ever emerging new data from the experiments, especially those related to (anti-)baryon production. In some cases these new objects like color ropes [25] or partonic clusters [26] are analogs for deconfined matter.

In the CERN-SPS energy domain the principal models used employ the "string" (a color field stretched between two partons) concept in various ways. For example, in the FRITIOF [28, 29] model hadrons can only exchange momentum (Pomeron exchange), while in VENUS [30], as in most dual parton models, they exchange both color and momentum. There are also hybrids, which include both string formation, and hadron excitation and cascading, such as RQMD [31] and its successor URQMD [32]. These combine classical transport with stochastic interactions, including the possibility of re-interaction for the produced secondaries [33]. The hadronic cascading mechanism is increasingly important at

BNL-AGS energies and below (ARC [34]).

At RHIC energy the situation is much cleaner than at CERN–SPS. The conditions for applicability of perturbative QCD during the very early stages of a collision is reached. Models taking into account the increasing role of perturbative QCD and hard processes, e.g. the parton cascade model VNI [38] and HIJING [39, 40, 41], have been developed. Calculations show that about half the produced particles are coming from "hard" processes. The perturbative cascade has to be followed by a hadronization model and then an evolution of the dilute hadronic phase. The first steps in this direction have been taken by coupling the URQMD hadronic transport model to a parton cascade [42].

Hadronic cascade models successfully described the general features measured in heavy-ion collisions. However, they failed to reproduce in detail the specific signals observed at SPS, most notably the Ω production [35, 36].

There have been many attempts to tune existing hadronic cascade models and to add new features to them in order to explain existing CERN–SPS data. Unfortunately, it is often the case that not enough attention is paid to the physical consistency of the model, especially at high energy densities. Little is known about these new features, and even less is known about their behavior in a dense environment. Müller in Ref. [37] even suggested that: "the codes based on such models must contain a flag that automatically generates a warning message when the limit of credible applicability of the hadronic cascade is reached (e.g. when strings begin to overlap), or when the final result depends essentially on fictitious components of the model that are not based on experimental evidence. The users of such codes would then know that the result is not a prediction of known physics but, at least in part, based on speculative ideas of its author." On the other hand, he pointed out that existing hadronic cascade codes are ideal tools for the description of the late stages of heavy-ion collisions, the chemical and thermal freeze-out of hadrons when the dense phase is over. These models can simulate hadronic evolution in a "normal" environment by two-body

interactions including known resonances. Therefore, for this purpose, they are superior to simple hadro-chemical calculations where only small deviations from thermal equilibrium are taken into account.

CHAPTER 2

The STAR Experiment

2.1 Overview of the Experiment

The STAR experiment is one of four experimental facilities at the Relativistic Heavy Ion Collider (RHIC) at Brookhaven National Laboratory. STAR and PHENIX are the two "major" experiments, while BRAHMS and PHOBOS are smaller scale spectrometers. STAR was designed and constructed to investigate the behavior of strongly interacting matter at high energy density and to search for signatures of QGP formation and chiral symmetry restoration. The initial STAR focus is on measurements of hadron production and the study of "global" observables which includes strange and non-strange particle ratios, yields, and spectra. The STAR physics program also includes a complete list of spin physics utilizing collisions of polarized protons at RHIC to measure the contribution of the spin of the gluon and of sea-quarks to the spin structure function of the proton. In this dissertation, we report results for collisions of Au + Au at $\sqrt{s_{NN}} = 130$ GeV from the STAR experiment in the first RHIC run in Summer 2000.

The layout of the STAR experiment is shown in Fig. 1. The initial configuration of STAR in its first run in year 2000 (when the data presented here was taken), consisted of a large Time Projection Chamber (TPC) for tracking, covering the pseudo-rapidity range (see Appendix for definition of variables) $\mid \eta \mid < 1.8$, and a Ring Imaging Cherenkov detector covering $\mid \eta \mid < 0.3$ and $\Delta\phi = 20^o$, inside a solenoidal magnet with 0.25 T magnetic field. The solenoid provides a uniform magnetic field of maximum strength 0.5 T for momentum analysis. Particle identification in the TPC was performed either via ionization energy loss measurements or pattern recognition of decays. The TPC has, by construction, full

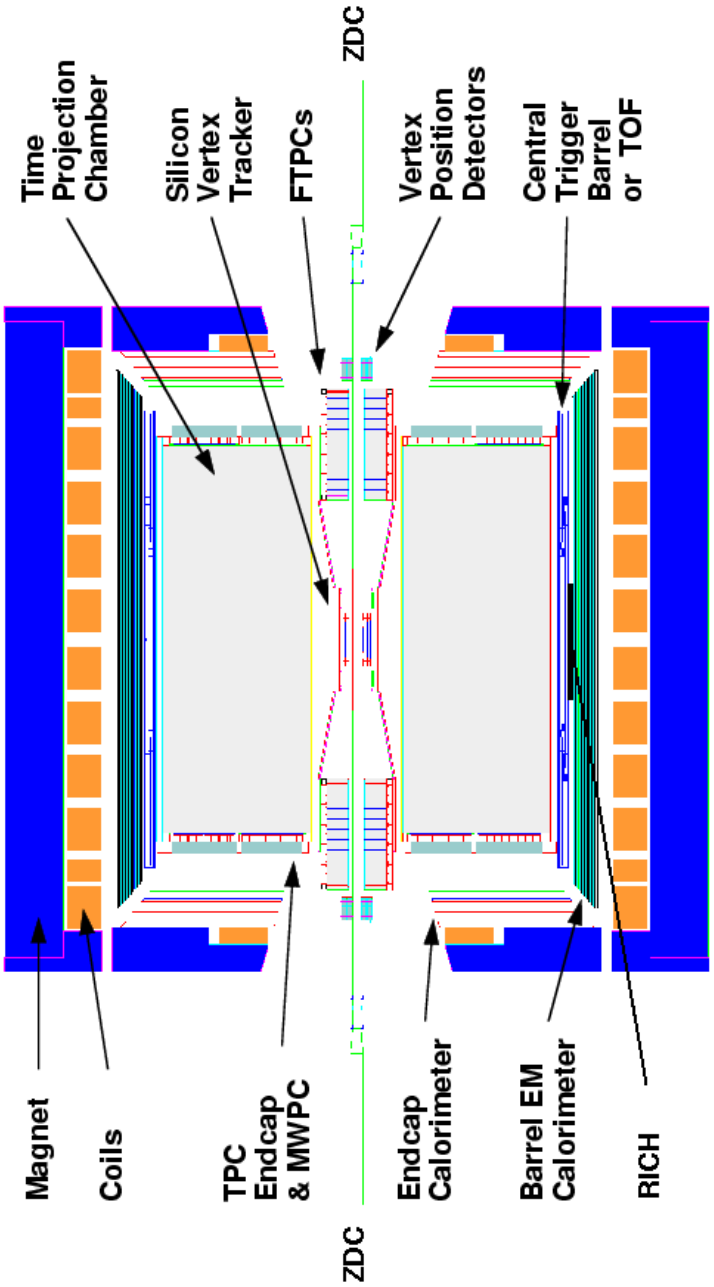

Figure 1: Side-view of the STAR experiment at RHIC.

azimuthal coverage ($\Delta\phi = 2\pi$).

2.2 The RHIC Facility

RHIC depends on many of Broohaven's world-class physics machines, which produce and accelerate the RHIC beams. The RHIC acceleration Complex consists of the following accelerators in order of beam travel: Tandem Van de Graaff, Booster, Alternating Gradient Synchrotron (AGS), and RHIC accelerator. Each of them acts as a 'booster' or pre-accelerator for the next one. The ions which are injected into the RHIC rings are fully stripped from their atomic electrons. The RHIC collider has a circumference of about 2.4 miles and it has two "lanes", two independent internal rings; the so-called "yellow" and "blue". Particles are traveling inside them in opposite directions. The two rings come together at six intersection points where the beams collide at almost 180 degrees and the physics studies begin. As we mentioned above, only four of the intersection points are instrumented with detectors (experiments). The typical design length of the interaction ('diamond') region is about 20 cm but in our data sample which was the first RHIC run the diamond had a Gaussian profile with a sigma of about 60 cm.

2.3 Beam and Trigger Conditions

STAR employs two complementary methods (two detectors associated) in order to be able to select events based on collision centrality. One method is based on triggering on particle production in the transverse direction relative to the beam and the other is based on looking for non-interacting nucleons, so called "spectators" in the forward–backward direction. The detector associated with the first method is called central trigger barrel (CTB) and the one associated with the second method is the zero-degree calorimeters (ZDC). The CTB, shown in Figure 1, is made up of scintillator slats and it surrounds the outer curved surface of the TPC. It measures the number of charged particles in the $\mid \eta \mid < 1$ region. The two ZDC's which are located at ± 18 meters from the TPC center and have

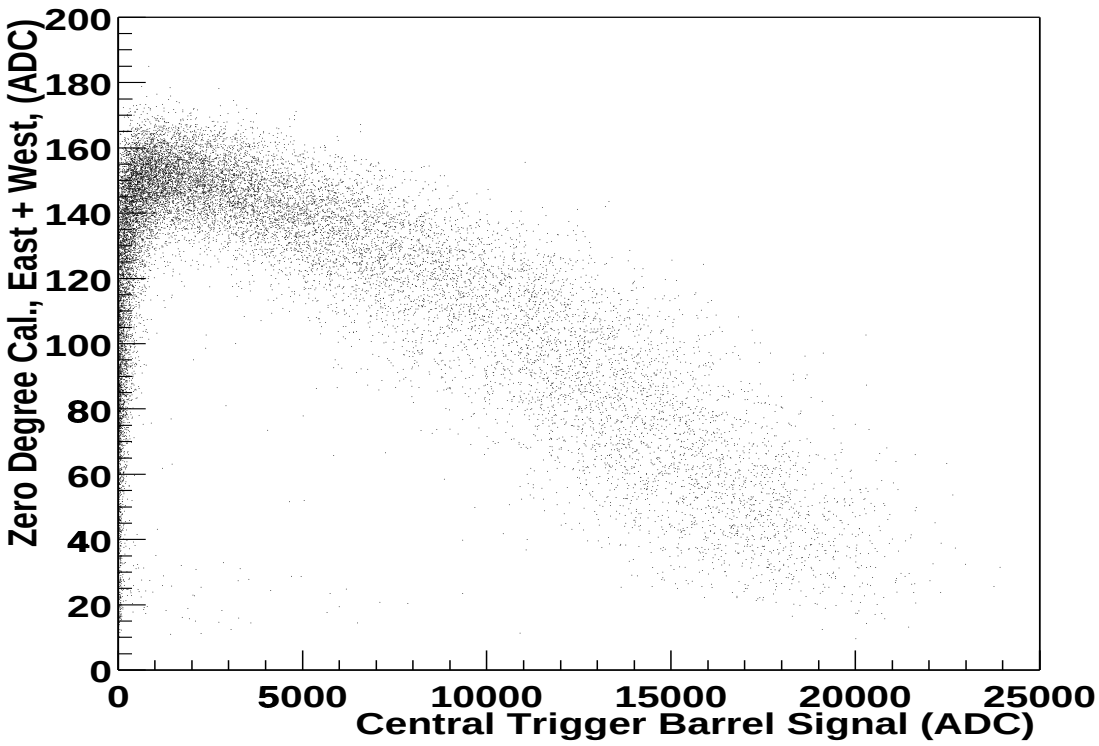

Figure 2: Correlation between pulse heights of Zero Degree Calorimeters (ZDC) and Central Trigger Barrel (CTB) in a minimum bias trigger.

an acceptance of $\theta < 2$ mrad measure the energy of neutral particles at 0 degrees, mostly spectator neutrons. Displayed in Figure 2 is the correlation between the summed ZDC pulse height and that of the CTB for events with a primary collision vertex successfully reconstructed from tracks in the TPC. This correlation is predominantly geometrical in origin. At large impact parameters, where the cross section is largest, only a few spectator neutrons are generated and the multiplicity in the central region is small, corresponding to low signals in both the ZDC and CTB. As the impact parameter decreases, the number of forward spectator neutrons grows rapidly, eventually saturating and then decreasing for small impact parameters. At the same time, the CTB multiplicity increases, with the most central collisions corresponding to high CTB multiplicity and a small number of forward

spectator neutrons. Thus, the correlation between the ZDC and CTB can be used to provide a trigger for collision centrality.

A "minimum bias" trigger (i.e. as unbias-ed as possible) was obtained by selecting events with a pulse height in each ZDC that was just above pedestal threshold. Triggers corresponding to smaller impact parameter were implemented by selecting events either by applying cuts in the ZDC signal (very central events) or selecting events based on the charge particle multiplicity in a certain $\mid \eta \mid$ region as measured in the TPC.

2.4 The TPC (Time Projection Chamber)

The Time Projection Chamber is the core detector of STAR. It has a large acceptance in pseudo-rapidity, $\mid \eta \mid < 1.8$, $p_T > 100 MeV/c$ and $0 < \phi < 2\pi$. The TPC is inside a 0.25 Tesla solenoidal magnet. The magnetic field is used to measure the curvature, and thus the momentum per charge of all charged particles reconstructed. Particle identification is achieved by measuring besides the particle momentum, the energy loss, applying topological cuts or constructing invariant masses.

The TPC is a cylinder of 4 meters in outer diameter, 0.5 meter inner radius, and 4.2 meters long. It is filled with a mixture of 90% argon and 10% methane and it is shown schematically in Figure 3. The tracking volume is surrounded by an electrostatic field cage which is built with 11.5 mm wide rings to uniformly step down the voltage from -31 kV on the central membrane to 0 V on the ground wires. The field cages are very thin : 0.62% radiation length for the inner field cage and 1.26% radiation length for the outer field cage.

Each side of the TPC is segmented into 12 azimuthal sectors. One sector is shown in Figure 4. Figure 5 includes a cross sectional view of the wire layers and pad plane. There are three layers of wires terminating each side of the chamber. The first layer is the gating grid which terminates the field cage voltage and is used to close the chamber when no trigger is detected. The second layer is the ground plane which captures the ions from the

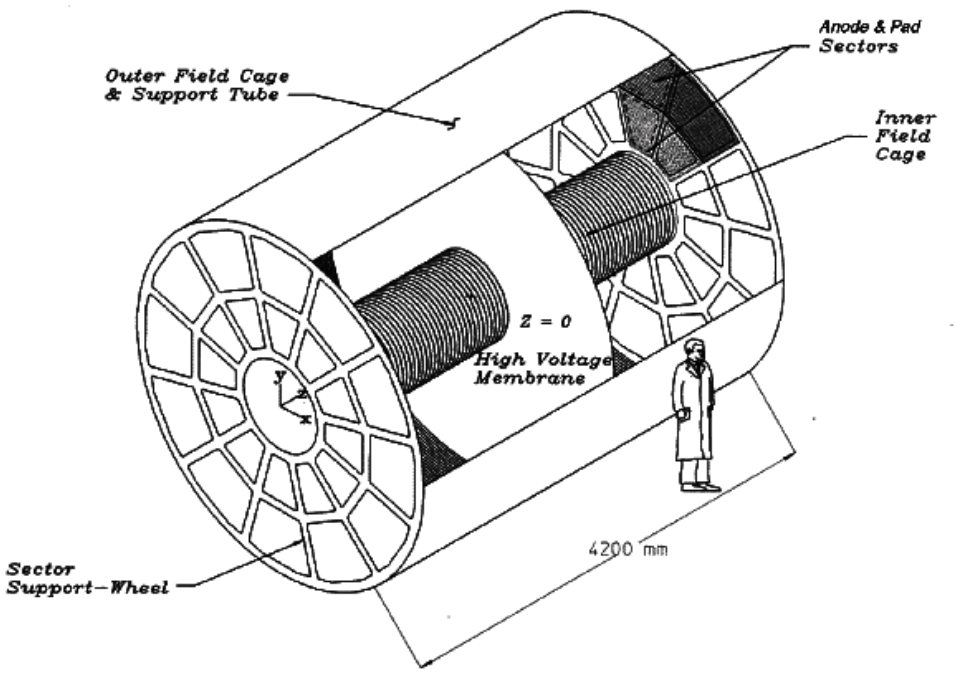

Figure 3: A schematic view of the TPC: showing the electrostatic field cage, the cathode in the middle, and the read–out pad planes on either end.

amplification region and the third layer is the anode plane. Gas amplification is achieved around each anode wire and the induced signal is picked up on the pad plane located under the anode wires. Each sector is divided into an inner and an outer part. The inner sector has 1,750 pads, each 2.85 mm wide (tangential direction) and 11.5 mm high (radial direction). They are grouped into 13 pad rows located between 60 cm and 116 cm from the beam line. The outer sector has 3,940 pads which are 6.2 mm wide and 19.5 mm high. The outer sector covers 32 pad rows between 127.2 cm and 189.1 cm radius. In order to keep the signal to noise ratio constant at 20:1 for both size pads, the anode voltages were set to achieve a gain of 1100 on the outer sector and 3000 on the inner sector.

The TPC has a total of about 136,560 channels and it samples longitudinally 512 times which gives a total of 70 million pixels.

The signal measured on the pads is processed using custom CMOS ICs. The arrival time of the electrons is sampled and read out into 512 time bins using a Switched Capacitor Array and ADC. The position of the particle along the drift direction is then reconstructed by converting from time bin to position by knowing the drift velocity. For a more complete description of the TPC, see Ref [43].

The TPC records and reconstructs the passage of all charged particles in the following (simplified) way (see also Figure 5). As charged particles traverse the TPC volume they ionize the gas and thus they leave behind an ionized trail (path). The produced electrons drift, due to the applied field, towards the anode wires, where they produce small charge avalanches due to high electric fields around the wires. Those avalanches induce charge images on the nearby pads which are read out electronically. These induced charges on the pads are then fitted with Gaussian functions and the x-y position of the centroid is determined. The time-of-flight, i.e. the time elapsed from the electron cloud generation to readout together with the known drift velocity of the cloud inside the chamber determine the position of the cluster along the TPC axis (z-direction). This way the full three dimensional 'picture' of the event is reconstructed. Details are given in the following chapter.

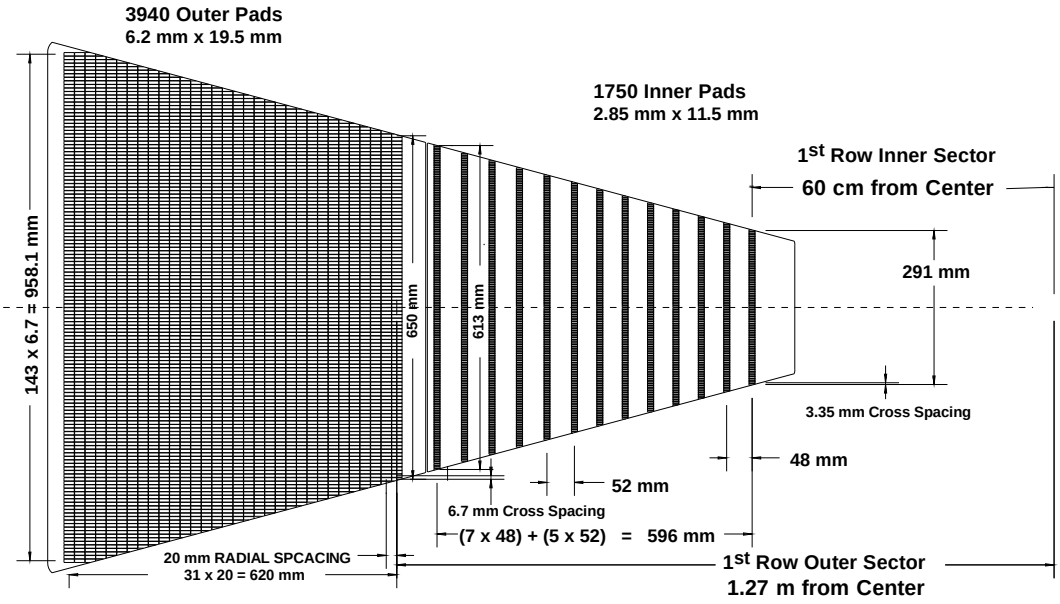

Figure 4: pad geometry.

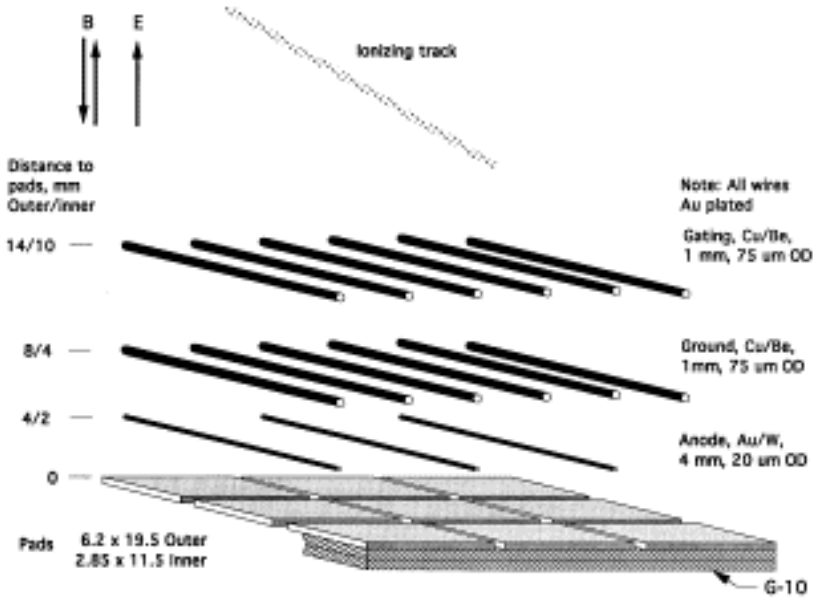

Figure 5: How TPC works.

CHAPTER 3

Event Reconstruction

3.1 Introduction

RHIC provides Au+Au collisions near the geometrical center of the STAR TPC. If any interesting event is identified by the trigger system, it is recorded on magnetic tapes by DAQ, the Data Acquisition system. This is called a "raw" event. Event reconstruction software is required to convert the raw input pixel data from either simulations or data from the experiment into a summarized list of the produced particles. The output of the event reconstruction software includes the momentum, energy, charge and/or particle identification (PID) of the individually identified tracks. Those are what our physics analysis relies on. To reach our physics goals, good performance of the event reconstruction software is essential. Event reconstruction software includes detector-specific calibration and distortion information which is necessary for particle reconstruction plus global software. This is where all the sub-detector specific information is merged into a comprehensive reconstruction of the triggered event.

The reconstruction chain (BFC) consists of a series of software packages (Makers) which perform a variety of different tasks, such as cluster finding, track finding and fitting, primary vertex location, primary track fitting and strange particle reconstruction etc. The output of bfc is written out as a reconstructed event into a Data Summary Tape (DST). The DSTs are the basis for any subsequent physics analysis.

Since the TPC is the main detector used during the Summer 2000 run, generating the data used in the dissertation, we will focus on the reconstruction done with the TPC. The task of the TPC event reconstruction is to reduce the raw data taken in a physics event

(about 7 million ADC values) to physically meaningful quantities such as a list of particle identities and momenta. Besides the raw data itself, the software utilizes geometry and calibration information, which are stored in a database. The method used of performing this data reduction is to examine pixel patterns on a padrow-by-padrow basis, finding locations where charged particles crossed the row, these positions are often called "hits." A tracking algorithm then links these hits together to find particle trajectories through the TPC. The particles are then identified by the characteristics of the tracks.

3.2 Cluster Finding in TPC

The STAR-TPC cluster/hitfinder is a software package, designed to extract from the raw data pad-row crossing positions ("hits") for charged particles that traverse the active volume of the TPC. The cluster/hitfinder is the first offline (non-calibration) software that will process the TPC data in the current model of data reduction. Almost all other offline software, including physics analysis software, build on the output of the cluster/hitfinder. Therefore, it is important that the general workings of this first software package are understood. Two modules, TCL and TPH, perform the cluster-finding and hitfinding, respectively.

The algorithm of TCL is based on building up a list of time-overlapping sequences by using each sequence in the list as a "seed" around which to search for overlapping sequences, which are then added to the list. Any sequence which is added to any list is marked as "used". The module identifies and stores clusters of pixels for each padrow by beginning from the "left-bottom" (= low pad number, low time bucket number), and searching until it finds an unused sequence, one which has not been associated with a cluster. This sequence becomes the seed. The algorithm looks in succession to the left and to the right of the seed for unused sequences which overlap with the seed. These are added to the list, later to become seeds. When clustering around the seed is finished, the next sequence on the list becomes the seed. When all sequences have been seed, the cluster list is complete, and the

seed for a new cluster is the first unused sequence looking again from bottom-left.

The cluster structures found by the cluster-finding module TCL are stored and passed to the hit-finding module TPH. It is the goal of TPH to locate padrow crossings of parent tracks, and to some extent to characterize the track (in terms of crossing angles and ionization left by the track).

The hit-finding algorithm is more modular than the cluster-finding algorithm described above, allowing improvements in any component of the process. This is important, as it is foreseen that improvements in the overall padrow crossing reconstruction efficiency will come from improvements in TPH (although improvements in speed may come as well in TCL).

Because of the high track density, there is a good chance that more than one hit can be found in a given cluster, especially on the inner padrows (see below). The "Mountain-finder" algorithm, described below, can be used to search for local maxima in the pad-TDC-ADC space. However, the search is not cheap in terms of cpu cycles (see below), and it is desirable to decide quickly whether a particular cluster is likely to warrant a search for multiple peaks. This decision is the first step in the TPH algorithm. A correlated plot of the RMS of the cluster in pad number and time bucket shows a clear division between clusters for which the Mountain-finder algorithm found a single hit, and those for which more than one hit was found. The position and orientation of the cut boundary may change with detector configuration (e.g. gas used, drift velocity) or improvement of the multipeakfinder, and so is specified by switch settings. After the peak(s) are found in the adc-tdc-pad space for each cluster, local hit position information is extracted from the pixels around each peak. These local positions are then translated into global x, y, and z coordinates.

Most tracking software is based upon fitting a set of space points (hits) with a functional form believed to represent a track. Thus uncertainties, as well as positions, are calculated and transformed to global coordinates. In order to obtain accurate and meaningful track

fit parameters (e.g. particle momentum), it is important that these uncertainties represent an accurate estimate of the width of the residual distribution. Track characteristics that determine the spatial resolution of a hit have been studied. These characteristics include the hit signal-to-noise ratio and the drift distance, which are available at the hit-finder level of analysis. However, the resolution is also strongly determined by track crossing angle, which is not well known until the tracking level of analysis. Therefore, only partial uncertainty information for each hit is stored in TPHIT(DX, DY, DZ). These uncertainties need to be modified at tracking time.

3.3 Tracking and Fitting

3.3.1 TPC tracking

The environment created in relativistic heavy ion collisions is quite unique and poses many problems not yet encountered in other collider or fixed target experiments. Two of the most important problems are the high track density and the low average momentum of the produced particles. The latter problem is characterized by multiple scattering and energy loss, which can significantly disturb the topology of the events.

Track formation is based on the track following algorithm. The algorithm starts at the outermost row of the TPC where the track density is at its lowest and then proceeds towards the inner rows using the position of the interaction point as a very loose guide. The track finding process contains the following steps:

Root formation: This step generates all possible 3-point links (point-to-point connections), or roots, starting at a given point. These roots serve as the foundation for the segment formation process. Criteria for accepting links as part of a root are set in a control table which is called tptpar.

Segment formation: This process tries to form a track candidate starting from a set of links that originate at the same point. Only the best candidate is kept and the points that

belong to it are marked as used, that is, they are removed from the available hit pool for segment formation. A helix track model is fitted to the selected points after each segment is formed.

Segment extension: This phase makes an attempt to associate more points with the tracks. A helix with parameters fitted in the segment formation step is used as a track model. All the points that are within a specified distance of this model are accepted, added to the segment, and removed from the available point list.

Spiral merging: Since low momentum particles lose energy causing their helix parameters to change along their length, a special algorithm must be applied to include these effects and allow for a successful identification of low momentum tracks.

3.3.2 Global Tracking and Reconstruction

The off-line global event reconstruction software correlates all the tracking, timing and energy deposition information from each detector in STAR and produces the final, overall reconstruction of collision events, selected by the STAR Trigger system, at the collision vertex, in the STAR global Coordinate System. The schema of global event reconstruction software is shown in Figure 1. The task we are facing at this level is to find the best way of combining the detector-specific pieces of information so that the resulting event summary closely resembles the actual particle production. In this spirit, the actual implementation of this level might include an iterative interaction between the various tasks, i.e. the use of PID information in Global tracking and vice versa.

The functionality needed at this level of integration can be divided into two parts: one is the need for correlating information from different detectors, and the other a set of service-routines which this level should provide to other tasks within the event reconstruction and/or calibration processes. It is apparent that in order for this global reconstruction software to work properly a close interaction with the central geometry and material data

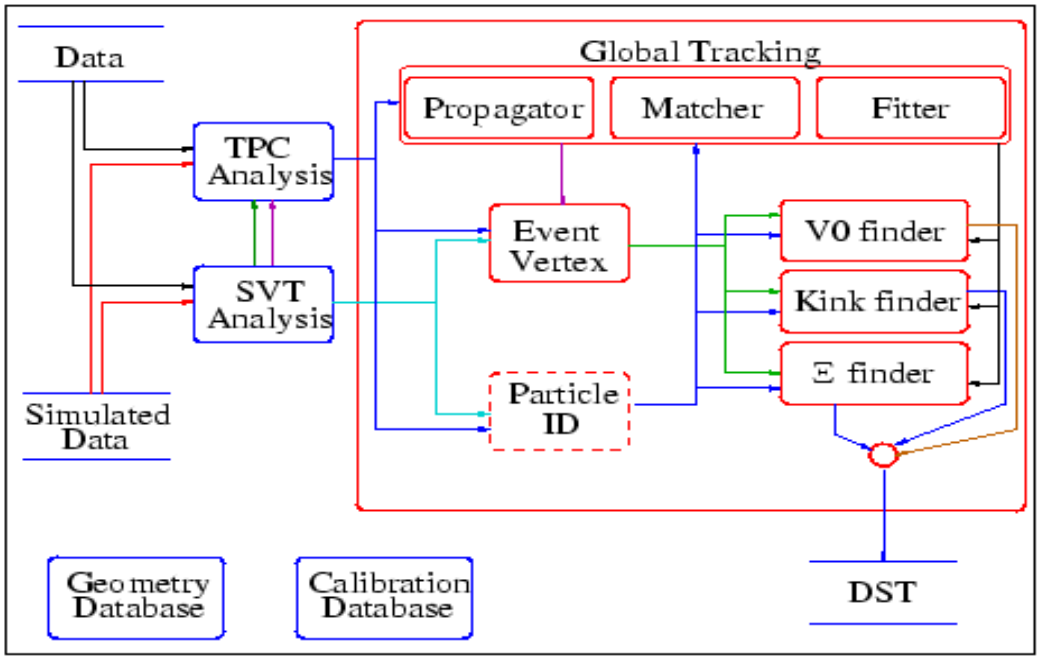

Figure 1: The STAR global event reconstruction chain

base is essential.

In the first group the need of the following tasks is identified: (1) Global tracking: This comprises two functions: Track and hit matching between different detectors, as well as refitting the matched points with or without the vertex hypothesis. The use of the event vertex as an extra point on the refitted track is important as it is going to improve the overall momentum resolution. At the same time the tracking input used in e.g. V0 reconstruction routines should not include the event vertex while refitting the SVT and TPC points. (2) Event vertex determination: Global tracks are the best input to a primary vertex finding routine. In general the resulting event vertex should be of better quality to the one determined by the TPC or the SVT alone. Special attention should be paid in the case of multiple event vertices (pile-up), as in p-p collisions. (3) PID assignment: Timing (TOF) as well as energy deposition in the TPC, SVT and EMC is combined and a probability of a PID is assigned to each reconstructed track. (4) V0 finder: Secondary vertices like

V0s are reconstructed at this level using reconstructed global tracks. Although part of the V0 search clearly belongs to the physics analysis level, the initial steps of V0 finding and fitting should take place during the event reconstruction since no reconstructed space-points are written on the DSTs, something a V0 fitting routine needs as input. (5) Kink finder: Charged kaon and pion one prong decays inside the TPC volume are reconstructed at this level using reconstructed global tracks. As with the V0 search this analysis is completed at the physics analysis level. (6) Global filter: This offline software acts as a track filter flagging all background tracks as well as tracks which are not related to the triggered event. (7) Event Summary: This comprises the function of producing the event DST as well as the transformation of the tracking information into a form more adequate for physics analysis (rapidity, Pt, CM frame, etc.). (8) Evaluation software: This includes all the routines and data stores needed for the evaluation of the performance of all the above software. This is an essential step in verifying that a particular module complies with the design specifications.

Ideally the performance of the global event reconstruction software is exclusively driven by the physics goals of STAR. This requires the precise knowledge of the sensitivity of, more or less, all STAR physics observables to the various resolutions and efficiencies of all involved software. The following parameters are considered at this level: (1) Tracking efficiency: This is the overall STAR tracking efficiency of the combined central tracking detectors, the SVT and the TPC, and it is the product of the individual tracking efficiencies and the matching efficiency as it is performed at this level. The individual tracking efficiencies have a strong momentum dependence which rises sharply for momenta up to 150-200 MeV/c and which then becomes constant at the 90-95% level. A similar behavior is shown by the matcher. Thus the product of all three currently results in an overall efficiency which is slightly lower than 90%, which is a quite acceptable efficiency. Another issue related to tracking efficiency is the percentage of so-called 'ghost' tracks in the final sample. These are tracks which are created either artificially or through segmentation of a single track. Our goal is

to have less than 10% (close to 5%) of these tracks in our final sample. This is the main function of the 'filter' module. (2) Momentum resolution: The momentum resolution is greatly enhanced at this level mainly due to the extended track length the combined track pieces have. For most momenta it has been shown to be at the 2% level which is adequate for almost all STAR observables. The only exceptions are the very high Pt probes where the determination of steeply falling exponential slopes in Pt might be compromised by low momentum resolution. The construction characteristics of the detectors set the limit in this matter and not software considerations. (3) Particle identification: The performance of the global PID software (which is nothing else but a mere combination of information from the individual detectors) is determined by hardware parameters as well as performance of the individual detectors and therefore all performance specifications are addressed at the individual detector level. (4) Event vertex resolution: The current performance is transverse and longitudinal resolutions of less than 100 microns for heavy ion events and for the combined TPC+SVT detectors and about 200 microns for the TPC alone which is much better than the average single point resolution of the individual detectors and adequate for the STAR flavor physics program. (5) V0, K efficiency: These are inclusive measurements and therefore the main concern is the reconstruction of a reasonable size of signal (in a certain number of events, usually being several thousands) with low levels of background.

3.4 The Kink Reconstruction

Figure 2 shows an example (real data) of a possible charged kaon "kink" decay. This event is from the Summer 2000 run and for clarity only 20% of the hits from the event environment are drawn in this 2-D projection.

The goal of this dissertation is to look for this type of decay pattern: a charged kaon decays into a charged daughter and a neutral daughter. TPC can't observe the neutral daughter, so we characterize this kind of decay as "kink" decay. The package which is

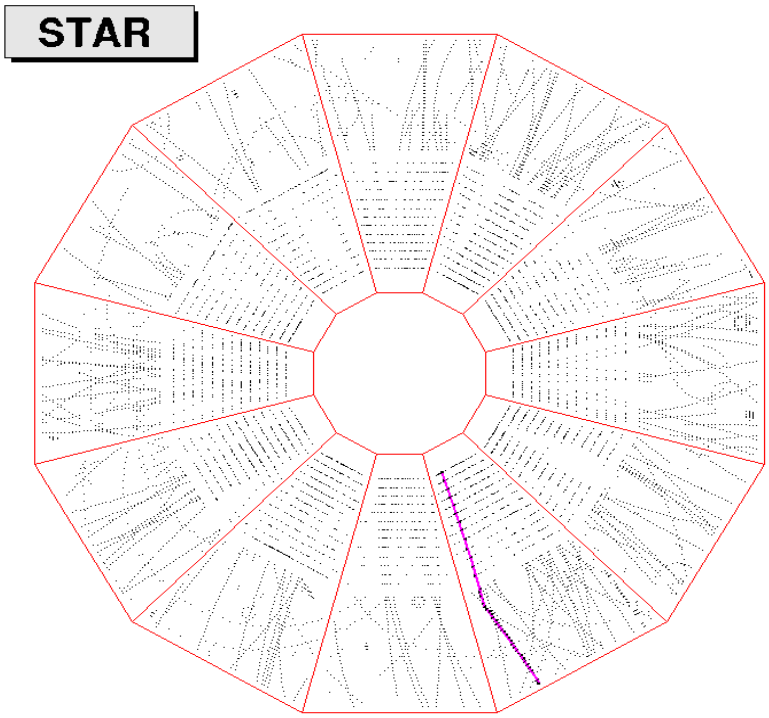

Figure 2: Charged kaon kink decay

responsible for searching the kink decay is called the kink finder.

3.4.1 The Kink Finder

The kink finder works by checking the hypothesis that any two global tracks intersect in space and in particular that where one track end the other one begins. There are about 3500 global tracks in one typical STAR central event. To avoid huge combinatorial background, it is decided that the kink finder looks for decays inside fiducial volume which is defined by 133 cm $<$ (the radius of decay vertex in x-y plane) $<$ 179 cm. This fiducial volume is exclusively in the outer TPC sectors which is densely instrumented and therefore a better region to perform the pattern recognition.

Based on the fiducial volume constraint, the kink finder starts by searching for candidate

tracks. First it checks if a track passes through fiducial volume. If it does it is rejected from the pool of tracks that later are paired together. It then checks if the track's 2D starting radius is smaller than the upper limit of fiducial volume, or the track's 2D ending radius is larger than the lower limit of fiducial volume. If it is, kink finder will keep it in a container.

After looping over all global tracks, kink finder obtains a container of kink-related track candidates. It then sorts the container by the 2D starting radius of track. Since the parent of a kink decay must have smaller 2D-starting-radius than that of the daughter, the parent of the kink must be in the front of the daughter in the container after sorting. In other words, we know which track is the parent track and which track is the daughter at the early stage of kink reconstruction. The kink finder then proceeds to check if two candidate tracks have the same charge signs. It requires that the impact parameter of the parent track must be smaller than a specified value, and the impact parameter of daughter greater than a specified value. The distance at closest approach (DCA) between the parent and daughter track must be smaller than some value. It also checks the distance between the last hit of the parent and the first hit of the daughter, and the distance between the last hit of the parent and the kink vertex candidate. In this way, accidental crossings in space as well as crossings of a X-type are rejected. The next step is to reconstruct the decay angle θ between the kaon and the daughter particle and see if it falls between the kinematical limits. An overall lower cut requiring $\theta > 1^0$ was applied, which helped clean the sample at the reconstruction level. When it finishes, it writes out the vertex and related track information to DST for further analysis.

3.4.2 Reconstruction Cuts

The cuts which are applied at the reconstruction stage are the following. The specific (listed) values where chosen after careful examination of the whole cut space and represent the optimum between signal preservation and maximum background rejection.

- Decay vertex should be in fiducial volume and both tracks should have the same charge. The fiducial volume is defined in the transverse (radial) direction and the cut is $133\,\text{cm} < R < 179\,\text{cm}$

- 3D distance of two tracks at the point of their closest approach (DCA), which is at the kink vertex, is less than the cut value of 0.5 cm.

- Decay angle should be greater than the cut value of just one (1) degree.

- The Parent should point (extrapolate) back to the event vertex (in 3D) and be within a radius of 2 cm.

- The Daughter of course should NOT point back to event vertex, it should be outside a radius of 2 cm.

- Decay kinematics should be close to a mass hypothesis. Energy conservation is allowed to be "violated" by a margin of 100 MeV. This is a resolution effect of course not a true violation.

- The distance of the last point of the parent to the first point of the daughter should be less than 14 cm in the radial direction and 20 cm in the z-direction.

- The distance of the last point of the parent to the kink vertex should be less than 14 cm in the radial direction and 20 cm in the z-direction. The same between the kink vertex and the daughter start point.

The Table 1 is a summary of all cut used for signal extraction during DST production.

Fiducial volume	(133., 179.) cm
Parent impact	$< 2.cm$
Daughter impact	$> 2.cm$
2D distance between parent last and daughter start points	$< 14.cm$
Z distance between parent last and daughter start points	$< 20.cm$
Z difference between projected points	$< 2.cm$
Decay angle	$> 1.degree$
Dca	$< 0.5cm$
2D distance between kink vertex and parent last point	$< 14.cm$
Z distance between kink vertex and parent last point	$< 20.cm$
2D distance between kink vertex and daughter start point	$< 14.cm$
Z distance between kink vertex and daughter start point	$< 20.cm$

Table 1: Summary of reconstruction cuts.

CHAPTER 4

Data Analysis

The input to this stage is the so called micro-DSTs which is nothing else but a summarized version of the DSTs. By summarized we mean that the STAR-DSTs are scanned and only the information which is relevant to this analysis is saved. This allows for a quick turn around time during the analysis so that the micro-DSTs can be analyzed (scanned) hundreds of times. As we have mentioned already during reconstruction we make an efforts to keep as much signal as possible without paying attention to the signal to background ratio. The purpose of the stage of the data analysis is to reduce the signal to background level while preserving most signal. Our goal is to further suppress the background contamination from initial levels of 300% down to less than 20%. The enhanced signal purity will then allow us to make distributions where the physics is dominated by real kaons with minor background corrections.

4.1 Analysis Cuts

To improve signal to background level, we have to apply more strict cuts. Simulation study suggests that the main sources of background are pion decays ($\pi^{\pm} \rightarrow \mu^{\pm} + \nu$) and two random track combinatorial background most of which is from spiraling electrons in the chamber. The pion decays are rejected by cutting on the decay opening angle and the electron contamination by cutting on daughter momentum.

Figure 1 shows the decay angle (θ), in degrees, as a function of momentum, for all decays. All analysis cuts have been applied to get this plot except the decay opening angle cut (which is plotted here). The narrow and densely populated band at low θ are pion

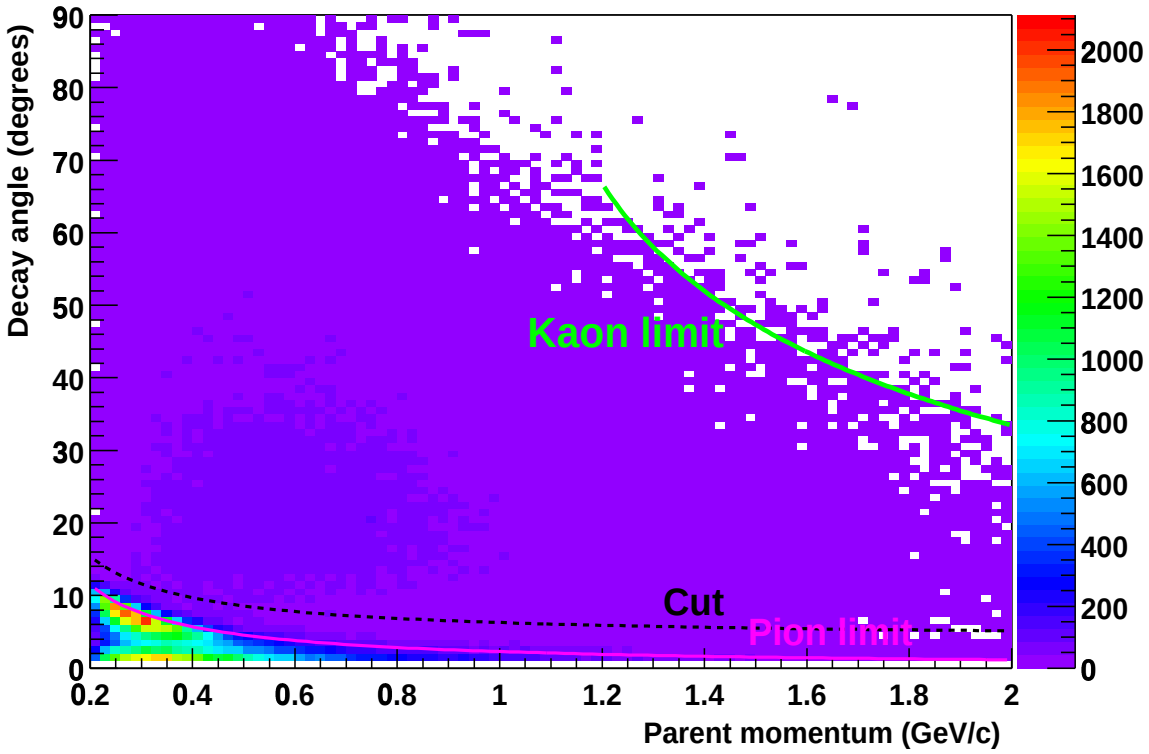

Figure 1: The decay angle vs. parent momentum

decays whereas the less populated band are mostly kaon decays. The separation between the two particle species is distinct. For a given momentum pions tend to have much smaller decay angles than kaons due to a combination of two factors: a) The Lorentz–boost factor $\beta\gamma$ is about 3.5 times larger for pions than for kaons of same momentum due to the mass difference. Since the decay angle in the lab system scales roughly as $\theta \approx 1/\gamma$, the pion decays are more forward focused than the slower kaons. Also, b) the muon momentum in the center of mass (c.m.) system (Q-value) for the kaon decay is 236 MeV/c as compared to 30 MeV/c for pions which also leads to a further smaller angle for the pions.

The line in Fig. 1 labeled "Pion limit" is the maximum decay angle which is kinematically allowed for the given momentum. We can see that this limit of the decay angle is a

function of parent momentum, so instead of applying a cut of a constant number, we use a variable cut which changes with parent momentum. Taking into account the effects of finite reconstruction resolution we chose to select this cut to be the kinematical limit plus 4 degrees. More specifically the cut which is implemented in the code has the following functional form which is found to best approximate the requested shape:

$$\theta < (atan(\frac{1}{\sqrt{636.284 \cdot p^2 - 1}}) \cdot 57.2958 + 4.) \tag{4.1}$$

where p is the parent momentum.

In the same figure the line "Kaon limit" shows the corresponding kinematical limit for the kaon decaying into a muon. The line stops at about 1 GeV since for kaon momenta below that the Lorentz boost is not enough to flip forward muons going backward and therefore there is no specific limit in the decay angle. One might wonder why there are a few counts above the kinematical limit line but remember that there is still some background left in the sample (which does not obey any decay rules) and also that there are other one-prong kaon decays (with smaller branching ratios) where the allowed decay angle is higher.

Figure 2 shows the distribution of daughter momentum and the position (value) of the applied cut. The peak close to zero is mainly due to combinatorial background involving a spiraling electron. This is another powerful way to eliminate background. The requirement for daughter momentum is that it is greater than $0.1 GeV/c$.

The combinatorial background is further reduced by cutting on minimum ΔE (more strictly enforcing Energy conservation), and the distance of closest approach (DCA) between parent and daughter tracks. In this analysis, we know the momenta of parent and daughter, we assume three kinds of decay modes (the major decay modes): $K^{\pm} \rightarrow \pi^{\pm} + \pi^0$, $K^{\pm} \rightarrow \mu^{\pm} + \nu$ and $\pi^{\pm} \rightarrow \pi^{\pm} + \pi^0$. We know the masses of decay participants and we calculate the momentum of the neutral daughter during the reconstruction of the decay (momentum conservation). This leaves us with one constraint, the energy conservation law.

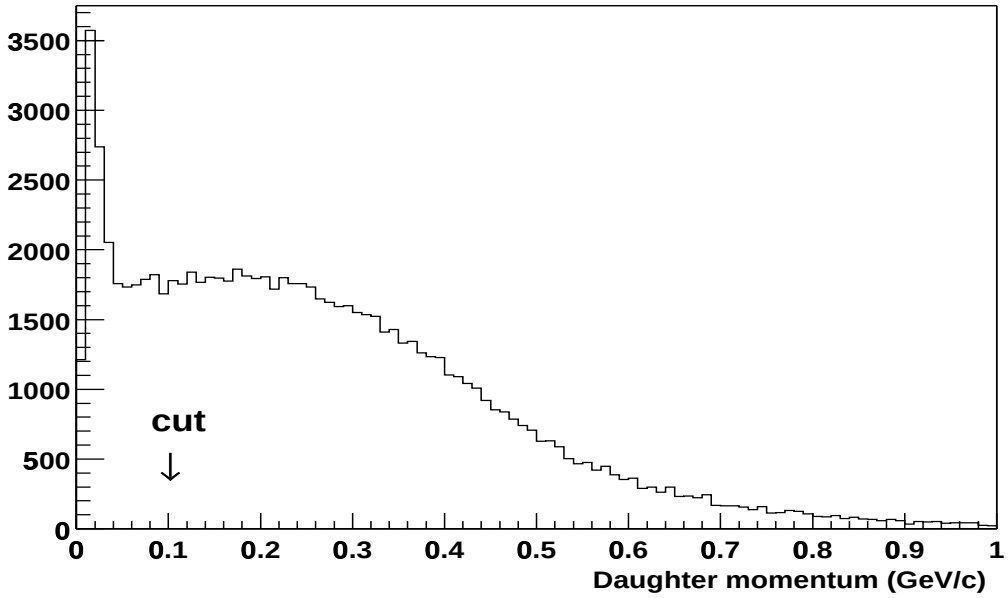

Figure 2: Daughter momentum

We can use this to either calculate an invariant mass for the parent, or by assuming the mass, to check the validity of the law. Here we use the latter one and therefore we form the absolute value of the difference between the two sides of the energy conservation equation. Since we check it for three kinds of decay modes, we have three numbers. The smallest one has the largest possibility to be real. A distribution of the smallest number which is called minimum ΔE can be made, as shown in Figure 3. Our analysis cut for this quantity is $0.05 GeV$.

Figures 4 and 5 show the dca distributions for both data and fully simulated HIJING events. Both show almost identical shapes for the total signal. The distribution shows a bump at low values as expected from any tracks having a common origin. In the ideal case it should be a delta function at zero but resolution effects smear it to a half Gaussian–like form. The dca distribution for the random combination of any two tracks should be flat, since there no actual correlation. This is shown in Fig. 5 with simulated events, where one

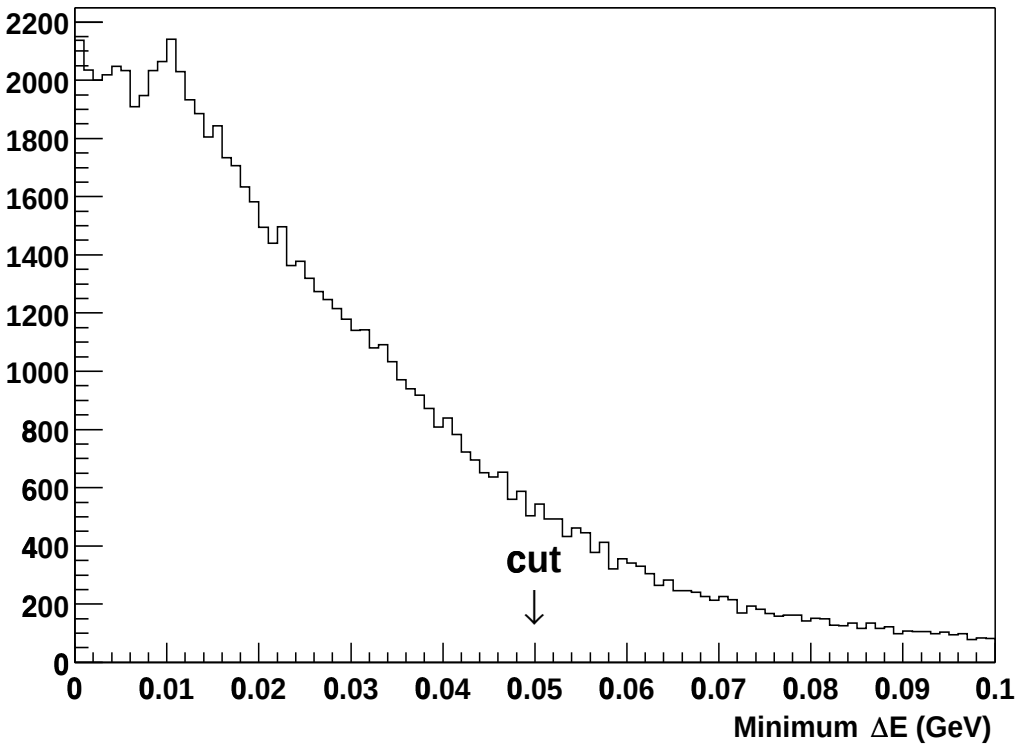

Figure 3: Minimum delta energy

knows what is what. The chosen value for this analysis cut is 0.25 cm (Fig. 4).

The distribution of dE/dx versus particle momentum has been made in Figure 6. All analysis cuts are applied before plotting this figure. The two dotted lines show the band where theory expects to have kaons. One sees that with the exception of a few counts the entire signal is within these limits. These limiting lines also represent the dynamic cuts which we apply in order to further clean the sample mainly from low momentum pion (lower left side), although this cut is a minor one.

After exhausting our cuts, the final background level is estimated to be 15–20%. All physics distributions are background corrected. Table 1 summarizes the applied analysis cuts.

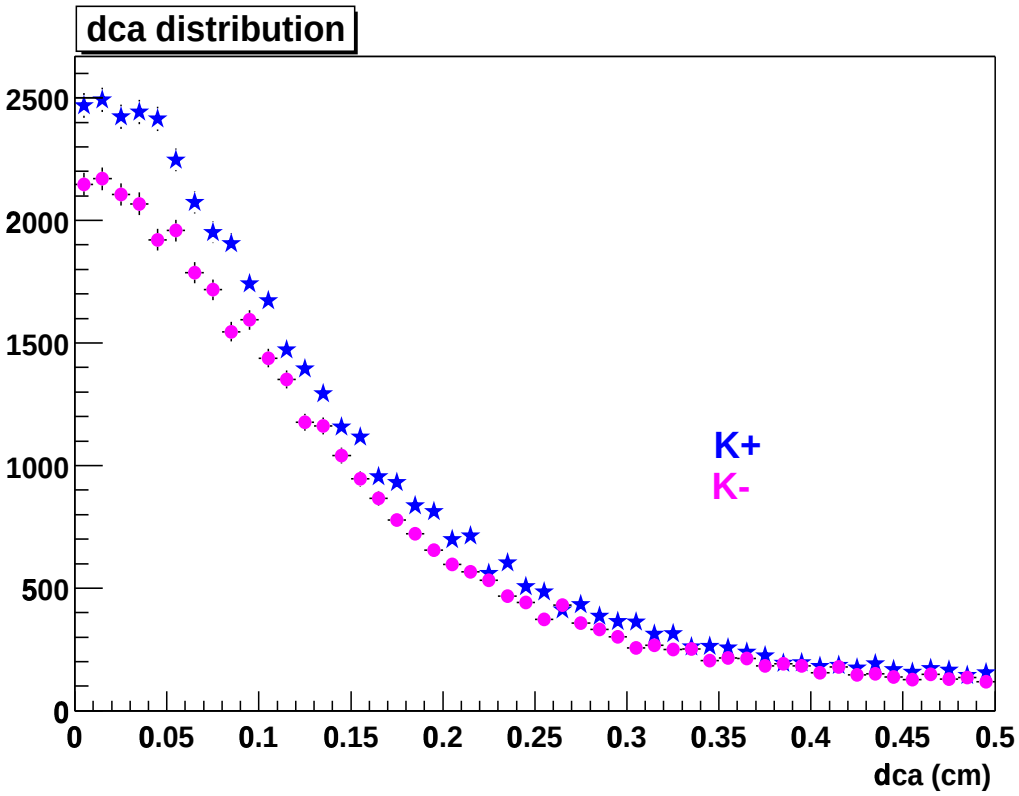

Figure 4: The distance of closest approach (dca) between parent and daughter tracks for data.

4.2 Corrections

Although the STAR TPC has larger acceptance compared to other similar detectors, it still does not have 4π coverage. Some particles which are generated from collisions do not enter the active volume of the TPC, so they can not be detected. This is a detector acceptance issue and the effect for central rapidities is very small, but still, it has to be accounted for when we estimate the kaon yields. As we mentioned already, we do restrict our analysis in a fiducial volume in the outer part of the TPC. This is another acceptance–like factor which we have to take into account, and it has mainly to correct for the fact that most charged kaons will decay outside our fiducial volume. This correction factor is large

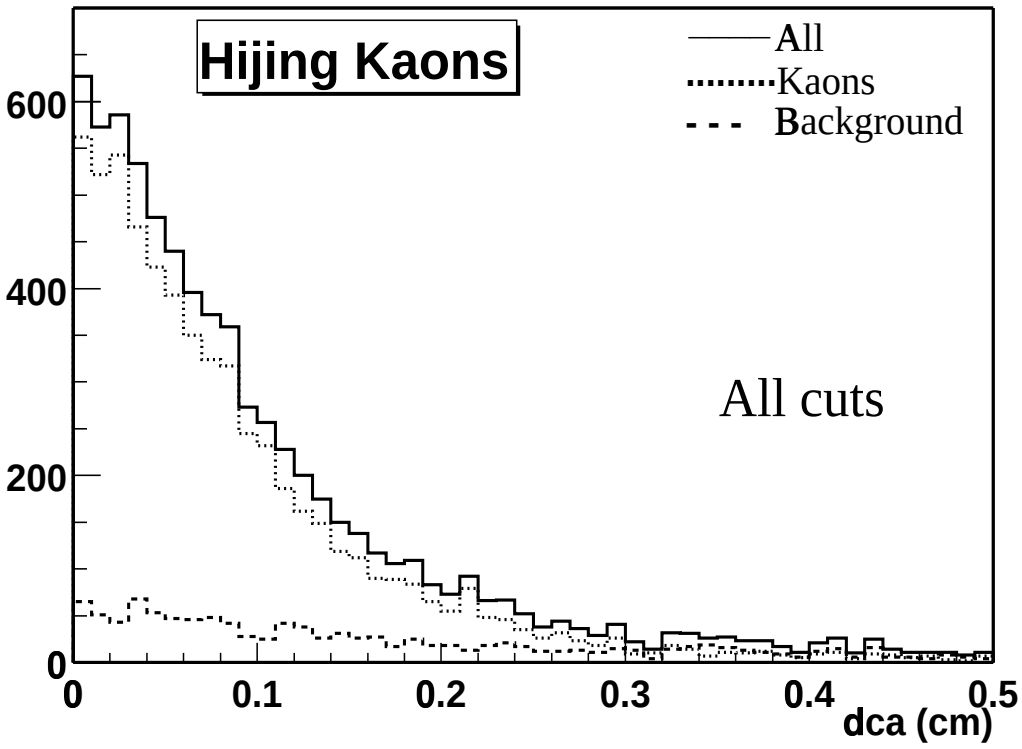

Figure 5: The distance of closest approach (dca) between parent and daughter tracks for simulated HIJING events.

(in the range 10–100) but it can be easily and very precisely estimated through a simple simulation.

There is also the problem of finite reconstruction efficiency. Cluster finding doesn't work perfectly everywhere, for example near the sector boundaries. Although the tracking software's performance is very good, still it is not 100% efficient. Finally, at the kink analysis stage and in order to reduce the background level, we have to apply some strict cuts. These cuts also cut off some signals. All of those effects should be considered and folded into a proper correction factor which is applied to the raw signal in order to derive the final particle yields.

In summary, the reconstructed data has to be corrected for geometrical acceptance

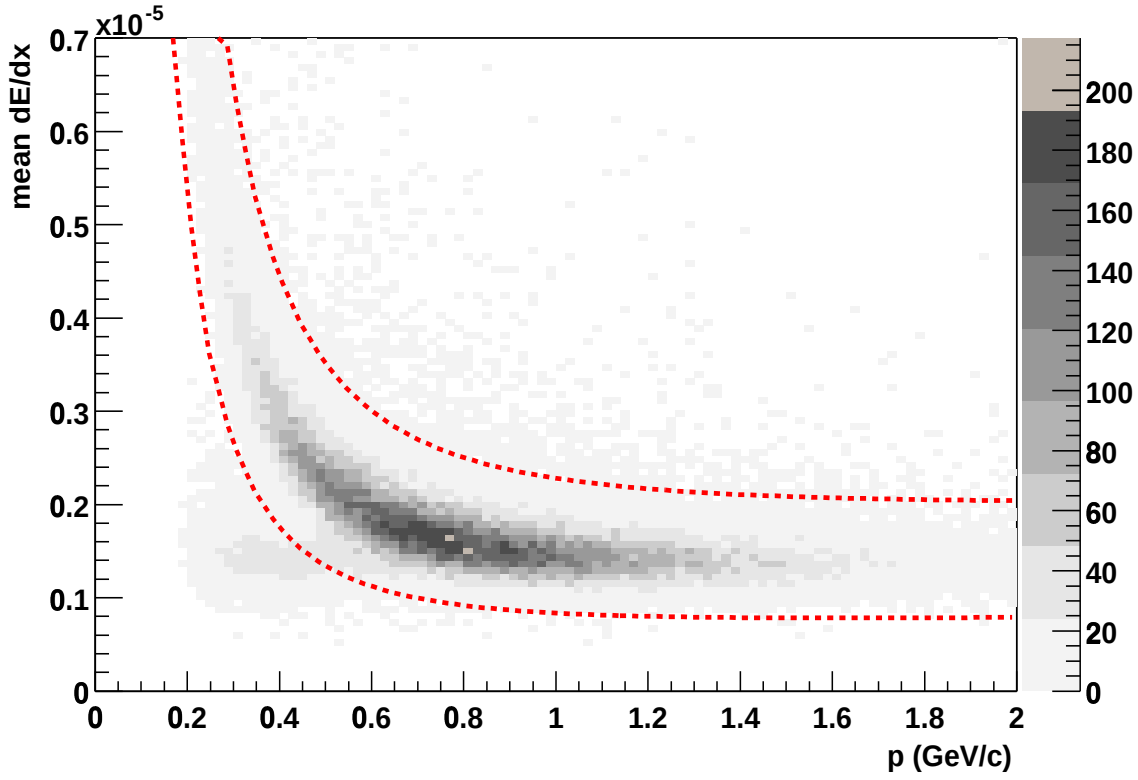

Figure 6: Particle ionization (dE/dx) versus the particle total momentum. The dotted lines indicate the region where kaons are supposed to be found.

and reconstruction efficiency. Figure 7 outlines in a simplified way this procedure and equation 4.2 summarizes the extraction of the kaon yield.

$$yield = \frac{data - background}{acceptance \times efficiency} \tag{4.2}$$

The unfolding of the data was done in small $y - p_T$ bins in order to be independent of the assumed distribution (input) used in the simulations. Therefore, for each bin in $y - p_T$ a correction factor was estimated which was then applied to the corresponding bin of the reconstructed data.

Corrected yields are obtained in each $y - p_T$ bin, where the number in each bin is

decay angle	See Figure 1
dE/dx	See Figure 6
daughter Momentum	$> 0.1 GeV/c$
ΔE	$< 0.05 GeV$
dca	$< 0.25 cm$

Table 1: Cuts implemented at the analysis stage

calculated from the formula given just above.

4.2.1 Simulation and Evaluation

Simulation is an indispensable tool to derive the physics results in detector experiments. It helps in the following aspects: (1) it is the unique way which people use to find the deficiency of detectors, hence obtain correction factors and use the factors to correct the experiment data; (2) it helps to understand the topology and background, so that better sets of cuts can be found to improve the signal to background level; (3) it helps to evaluate the performance of reconstruction software, so as to optimize the reconstruction software.

There are two categories of simulations: (1) event simulation (generator), i.e. simulates what happens in a real event. People put their theories and their speculations into simulation. For RHIC collision events, several models have been proposed and implemented. HIJING is the most popular one, (2) detector simulation. This simulates how detectors respond to the particles which are generated from the event. In STAR, there are two kinds of simulators for the TPC: tpc response simulator (TRS) and tpc fast simulator (TFS). The TRS package simulates the response of the TPC detector gas volume and electronics to the passage of ionizing energy through the TPC volume. Physical processes to be simulated by TRS are the drift of the ionized electrons in the gas, amplification on the sense wires, induction of signal on the readout pads, and the response of the readout electronics which

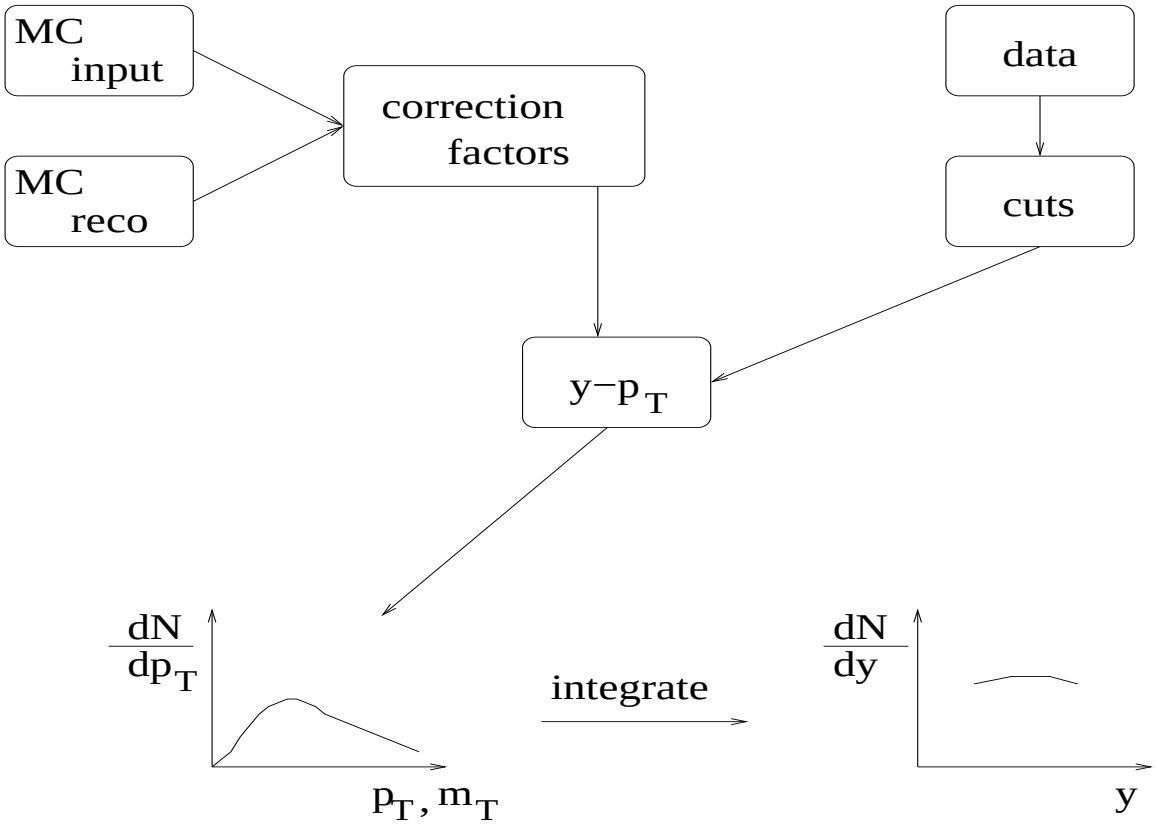

Figure 7: Spectra Analysis

generate digitized data. TRS is a very detailed simulator, so it is cpu-intensive. Sometimes, we need large volumes of Monte Carlo event samples in a very short time, this is why TFS is there. TFS directly generates the space points which have characteristics as close as possible to those hits reconstructed from real pixel data, thus bypassing the slow TPC simulator and the cluster finder/space point reconstruction analysis. A GEANT [52] Monte Carlo program takes tracks from an event generator and propagates them through the TPC, generating hits corresponding to each pad-row crossing. These GEANT hits are fed into the TFS as input. The output of TFS then forms the input of the STAR TPC tracking system.

The first step to evaluation is to relate the information from Monte Carlo events to

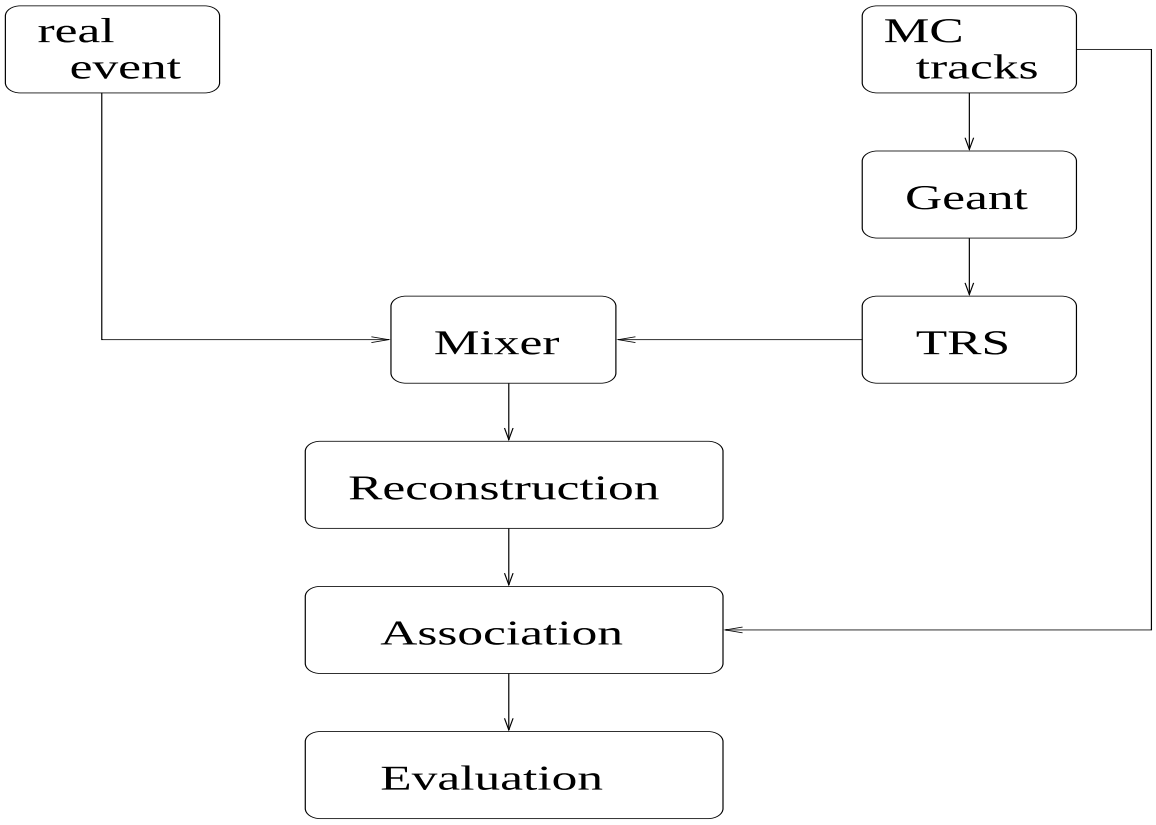

Figure 8: Embedding Logic

the information from reconstructed events. In STAR, this functionality is realized by the StAssociationMaker package. The relationship is established through multi-maps. There are several levels of associations: (1) the first one is the hit association which is done through proximity matching between Monte Carlo hits and reconstructed hits, where users define the distance criteria. (2) Then there comes the track association. Users define the criteria for the required number of common hits. It checks how many hits on a MC track match those on a reconstructed track. If it satisfies the criteria, we think that tracks are associated. (3) Vertex association is based on track association. Its criteria depend on particle decay topologies. For kinks, what happens in the StAssociationMaker is that it checks whether daughter tracks are associated, then whether the start vertex of the daughter track is not

the primary vertex, and then whether parent tracks are associated. In the kink analysis stage, we check whether the vertex is a weak decay vertex. Based on the three levels of association, we can proceed to do evaluation: for example, to see the hit position resolution, momentum resolution etc. Evaluation provides useful information to tune reconstruction software.

4.2.2 Embedding Procedures

GEANT-based simulations of HIJING events are crucial to the understanding and optimization of the environment but not for the calculation of acceptance and efficiency corrections. This is because no matter how realistic the simulation is, it cannot account for effects only existing in real data, e.g. dead channels, noise, collider background etc. What we do in this case is to put particles (embed them) into the real event environment and see how many of them we can get back after reconstruction. In this analysis, we know how many $K-$ we put into the chain, how many of them decay in the fiducial volume, and how many of them get reconstructed and survive our cuts. With this information at hand, acceptance and efficiency can be derived easily.

Knowledge of the STAR geometry and how a specific type of particle decays are already in the STAR knowledge-base. Also we need real raw event (daq) and event reconstructed information (DST).

Once the embedding chain gets the event vertex position and multiplicity of the event from DST, it can start to generate particles at the event vertex. In our case, the number of embedded kaons is 5% of the multiplicity. The reason that we choose 5% is that we want to put simulated tracks to the real event environment but don't want to cause any visible impact to it. The transverse momenta and phase-space positions of the generated particles are randomized, but the overall distributions are controlled by the input to the embedding chain.

Each particle goes through the simulated STAR geometry. It decays randomly according to their decay properties, a decay vertex is located and daughter tracks are generated. The number of padrows each track would pass, so how many hits would be induced can be determined.

Simulated particles are tracked through the STAR environment in the same way as real particles. Points from simulated tracks may then be converted into the same format as the raw data. From there, the simulated particles can be reconstructed together with real event particles using the standard reconstruction chain. If the simulated data shows similar observable distributions as what are in the real data, then corrections computed from the simulated data can be applied to real data to obtain real physical results. With simulated data, the initial number of generated particles in each $y - p_T$ bin is known and this information is required to calculate the correction factors. Details of data simulation, the acceptance correction, and the efficiency calculation follow.

4.2.3 Acceptance Calculation

The acceptance for K^- in the $y - p_T$ space is a product of several factors: a) the geometrical acceptance, b) the decay probability, and c) the effect due to the fiducial volume restriction. Figure 9 shows the overall acceptance. It is calculated as the ratio of the number of decays inside our TPC fiducial volume in a certain bin to the number of input particles. The region of $-0.5 < y < 0.5$ and $0.2 < p_T < 0.8$ GeV/c has better acceptance due to the TPC geometry and better performance of the reconstruction software.

4.2.4 Reconstruction Efficiency Correction

The efficiency is also a product of several factors: a) the hit reconstruction performance, b) the track reconstruction performance, c) the kink reconstruction performance which is nearly 100% and d) strict cuts in order to improve the signal to background level. Figure 10 is a combinatorial effect of the former three factors. Figure 11 shows the overall efficiency

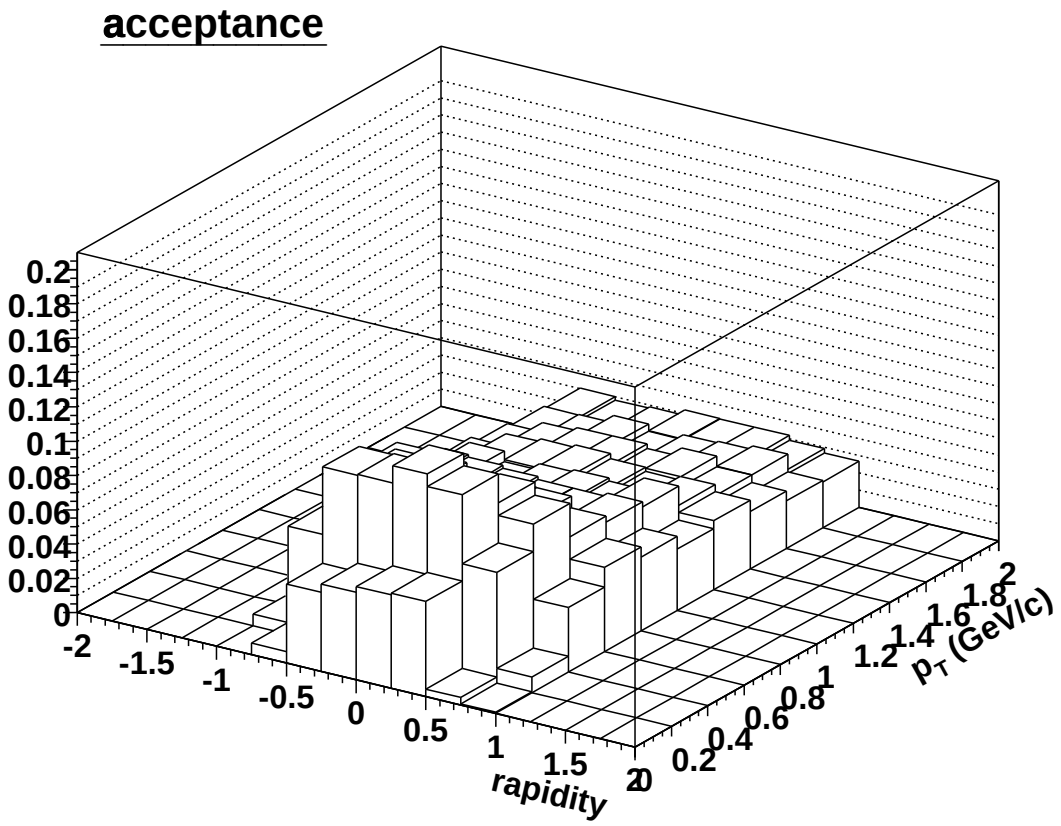

Figure 9: Acceptance

level.

4.3 Resolution of the reconstructed parameters

We define the resolution as the result of subtracting the reconstructed quantity from the corresponding Monte Carlo quantity.

Figure 12 shows the resolution of three reconstructed quantities at the kink vertex. The RMS for our two dimensional (radial) kink vertex resolution is 5.5 millimeter but the central Gaussian sigma is much lower than that, and the RMS in Z is 2 millimeter. The mean value for the decay angle resolution is 0.2 degrees with an RMS value of one degree. It appears

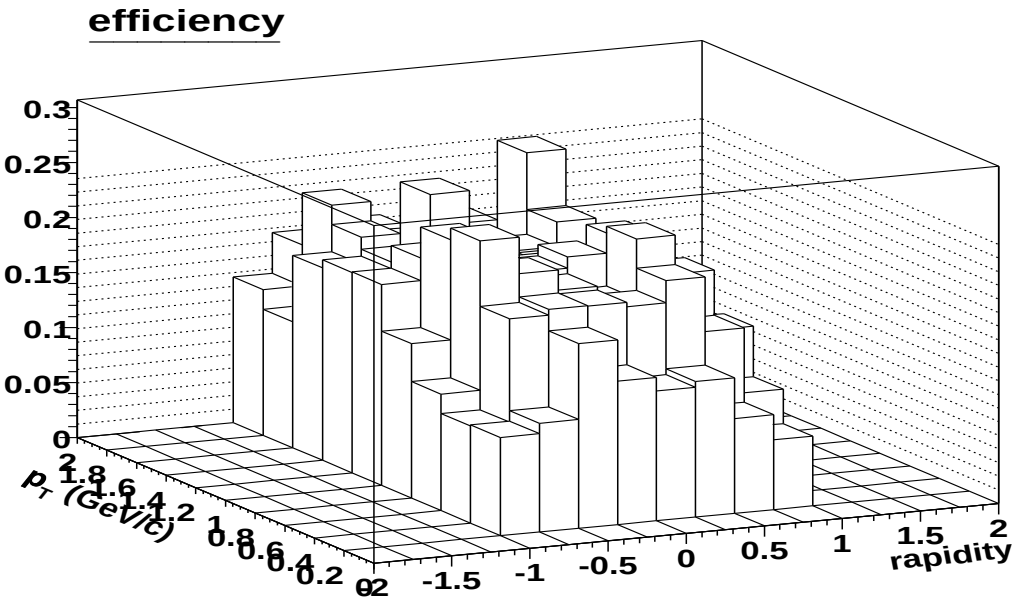

Figure 10: Efficiency

that we tend to slightly underestimate the decay angle. There is an explanation for this effect. The TPC tracking starts with hits at the outermost padrow. So the kink daughter track gets reconstructed first. It is very likely for the daughter track to pick up one or two hits which belong to the parent track. This will cause the daughter track fit to twist a little bit towards the parent track, so that the reconstructed decay angle will be smaller than what it should be.

Figure 13 shows the reconstructed quality of kaon tracks as seen by the kink. The RMS for relative p_T resolution is 6%. The plot in the middle is Δp_T vs. p_T. The rapidity resolution distribution centers around zero with an RMS is 0.007. We need this information when we show p_T, m_T or rapidity distributions because the choice of the bin size has to be more than the RMS values in order to avoid smearing.

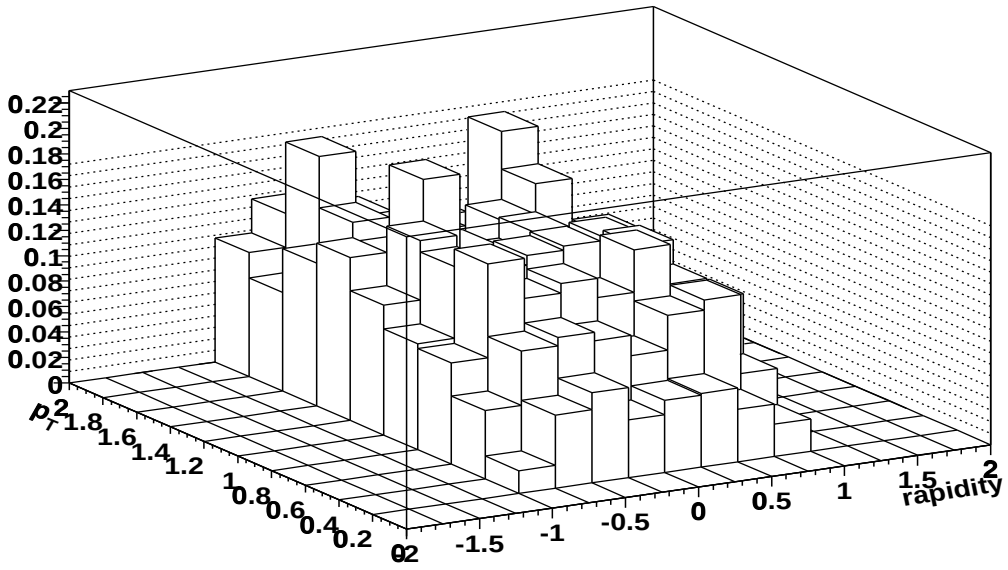

Figure 11: Efficiency after cuts

4.3.1 Background study

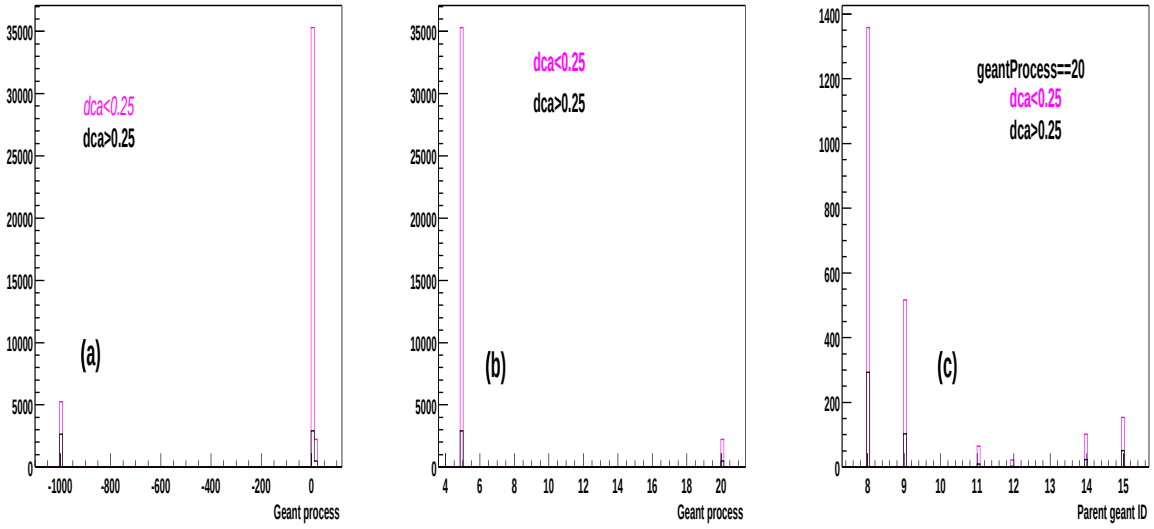

We did a background study with HIJING gstar data by running this chain: *simulation* → *reconstruction* → *association*. Three plots are presented above. The distributions were

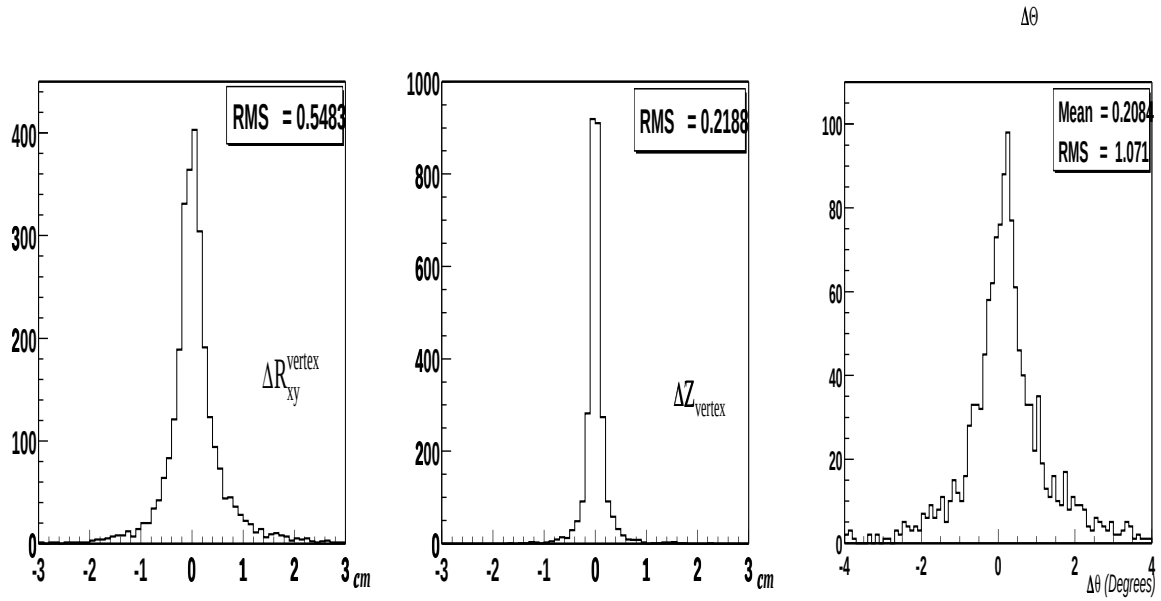

Figure 12: Kink vertex resolution in R (left) and Z (middle) directions plus decay angle resolution (right).

made with the data after we applied all cuts. In plot (a), we see two peaks. The lower peak is what we reconstructed which is not associated with any MC partner. So they are not kaon decays, and most probably they are the combinations of any two random tracks. Plot (b) is the magnified view of the higher peak in plot (a). The higher peak in plot (b) corresponds to the weak decay process (5), the lower peak hadronic interacting process (20). Further analysis with the weak decay process shows that they are kaon decays, since pion decays were eliminated by our decay angle cut. Plot (c) is the magnified view of the lower peak in plot (b). Those are hadronic inelastic interactions, which are the result of particles scattering with gas or material and leaving two tracks which are kinks topologically. From the GEANT ID distribution, we see that we have hadronic interactions of pions, kaons and protons.

After background subtraction, the background level is estimated at $\sim 10\%$ for HIJING

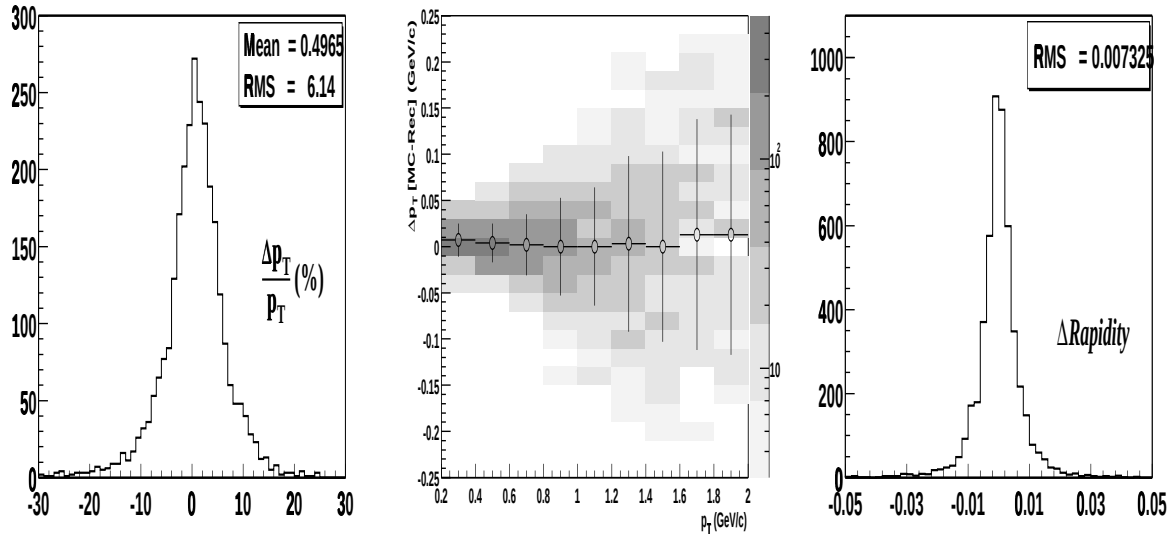

Figure 13: Kaon pt (left and middle) and rapidity resolution (right).

simulation. For real collision data the environment tends to be more noisy, so the background level is higher than that in simulation, but should not exceed 20%.

4.4 Are we reconstructing real kaons?

For collision data, one question arises: how do we know that we are actually reconstructing kaons and that we are not "making-up" some signal through the application of all these cuts? For simulation data, after running reconstruction, we obtain kink candidates. In this case life is easier since by comparing with the input signal we can "see" if what we reconstruct are real kaons. In these simulation studies, we find that almost 90% of the candidates are real kaons but there are several other plots that provide strong evidence that this is the case also for real data. We do list some of these below. Of course, the ultimate test is the resulting physics and how it compares with other measurements in other experiments or how it compares with kaons identified by dE/dx in the STAR TPC. We will discuss this part later, but we can say right now that the agreement between the various measurements

is remarkably good.

4.4.1 Dca distribution

In Figure 4, as the dca goes from 0.5 cm to 0.25 cm, the distribution is relatively flat. But as the dca decreases further, the curve increases linearly. This is clear evidence of a correlated signal, manifesting that parent and daughter tracks intersect at a single secondary vertex. It could be that this correlated background is coming from other sources that mimic the signal (e.g. hadronic interactions with a single charged particle in the final state), so one has to investigate further.

4.4.2 Invariant mass

Figure 14 shows the invariant mass distribution assuming $K^{\pm} \rightarrow \mu^{\pm} + \nu$ for both real data (top part) and simulated HIJING events (bottom part). All analysis cuts were applied with the exception of the ΔE cut, since we can only use the energy conservation equation once. We can see three peaks clearly. One of them is at 0.49 GeV which is the right position for the kaon mass. This is for the decay mode $K^{\pm} \rightarrow \mu^{\pm} + \nu$, and for that our assumption is correct. The other two peaks correspond to the decay modes: $K^{\pm} \rightarrow \pi^{\pm} + \pi^{0}$ and $K^{\pm} \rightarrow \pi^{\pm} + \pi^{\pm} + \pi^{\mp}$. Since our assumption is wrong for those two cases, we get the wrong mass position. But they do signal the existence of these decay modes. These can be clearly seen in the simulation which reproduces in an exact way not only the overall shape but also the specific position and relative composition (which is related to relative branching ratios) of the distribution. This provides strong evidence that the 'correlated' signal we discussed above had the decay features of kaons!

4.4.3 dE/dx vs. momentum

Another direct evidence of the integrity of the kink data is Figure 6. There the reconstructed signal shows ionization behavior which is compatible with the kaon hypothesis. Of

course the band extends into the high momentum region (minimum ionization) where pions and kaons merge, but in the region where the band should be clearly separated (momentum below 0.5 GeV) the signal smoothly follows the kaon line.

4.4.4 Life time

Figure 15 is the reconstructed signal's life time distribution in its rest frame. The raw distribution has been corrected for acceptance and other inefficiencies with factors which were obtained from embedding. The resulting distribution is then fitted and an experimentally determined lifetime is obtained. The ratio of measured lifetime to the 'Particle Data Booklet' value turned out to be $\tau_k/\tau = 0.97 \pm 0.11$. This means that the reconstructed particles are decaying with a lifetime which is characteristic of the charged kaons. This is another very strong evidence that the reconstructed signal is indeed kaons.

4.5 The alternative (dE/dx) technique for kaon reconstruction

In STAR two types of techniques have been used to identify charged kaons. The alternative to the one which is presented in this dissertation is called the energy loss (dE/dx) method. See Figure 16.

The dE/dx method for identifying charged kaons is achieved by measuring the mean energy loss, $< dE/dx >$, of charged particles in the TPC gas. The distribution of $ln[< dE/dx > / < dE/dx >_{BB}]$ (where $< dE/dx >_{BB}$ is the expected Bethe-Bloch value) for each centrality and p_T bin is fitted to four Gaussians corresponding to π, K, $e^-(e^+)$, and p ($\bar{p}$). The kaon raw yield is extracted from the fit results. Tracks are selected on the basis that they originate from the primary interaction vertex. They were required to have at least 25 (of 45 maximum possible) hits. A 75% truncation was applied to the measured dE/dx samples in order to reduce the effect of fluctuations in the ionization distribution. The drawback of this method is: 1) for $p_T \geq 0.8$ GeV/c, it doesn't work at all because pion, kaon and proton bands are merged, they are not distinguishable. 2) for $p_T < 0.8$ GeV/c,

it still suffers contamination from pions and electrons in some areas. For $p_T < 0.5$ GeV/c where kaons are well separated from other species, we estimate a point-to-point systematic error of 5% on the extracted kaon yield. For $0.5 < p_T < 0.7$ GeV/c where kaons and e^- (e^+) overlap in $< dE/dx >$, we parameterize the e^- (e^+) yield using knowledge from the lower p_T bins, and estimate the systematic errors on the extracted kaon yields to range from 10% to 20%. For $0.7 < p_T < 0.8$ GeV/c where kaons significantly merge with pions in $< dE/dx >$, we neglect the e^- (e^+) contributions, and estimate the systematic errors on the kaon yields to be on the order of 15%.

The advantage of the dE/dx method is that it doesn't require so large event statistics as the kink method.

4.5.1 Systematic error estimation

To estimate the systematic error, we have looked at two sources: 1) cut variable variation, 2) east/west TPC systematics.

When we investigated different cut values, every time we only changed one variable and kept the rest untouched (i.e. the same as our standard cuts), and then repeated the same procedure to deduce the rapidity yield and the inverse slope. Four kinds of variations have been checked. They are: 1) $dca < 0.15$ cm, no background subtraction, 2) $\Delta E < 0.025$ GeV, 3) "squeezing" the fiducial volume 143 cm ¡r¡169 cm, 4) $\mid rapidity \mid < 0.25$. Those analyzes showed a 4% spread for yields and 3% for slopes.

Possible detector effects for the TPC have been checked by separating collisions in the east TPC from the west and making sure no candidate tracks cross the central membrane. This study showed 1% variation for yields and 3% for slopes.

The SVT water manifold was not installed at the experiment when the year 2000 data was collected, but due to an oversight it was placed into the simulation. The water manifold affected our efficiency calculation. This had to be accounted for when we reported our

results. We did see a 4.5% effect in the corrected yield ratio of manifold/no-manifold by selecting on the z component of event vertex position. From this, the estimated net effect in the reported yields is about (or less than) 1% overestimation. The slopes were unaffected.

In summary, it is adequate to quote a 5% systematic error for yields and 6% for slopes.

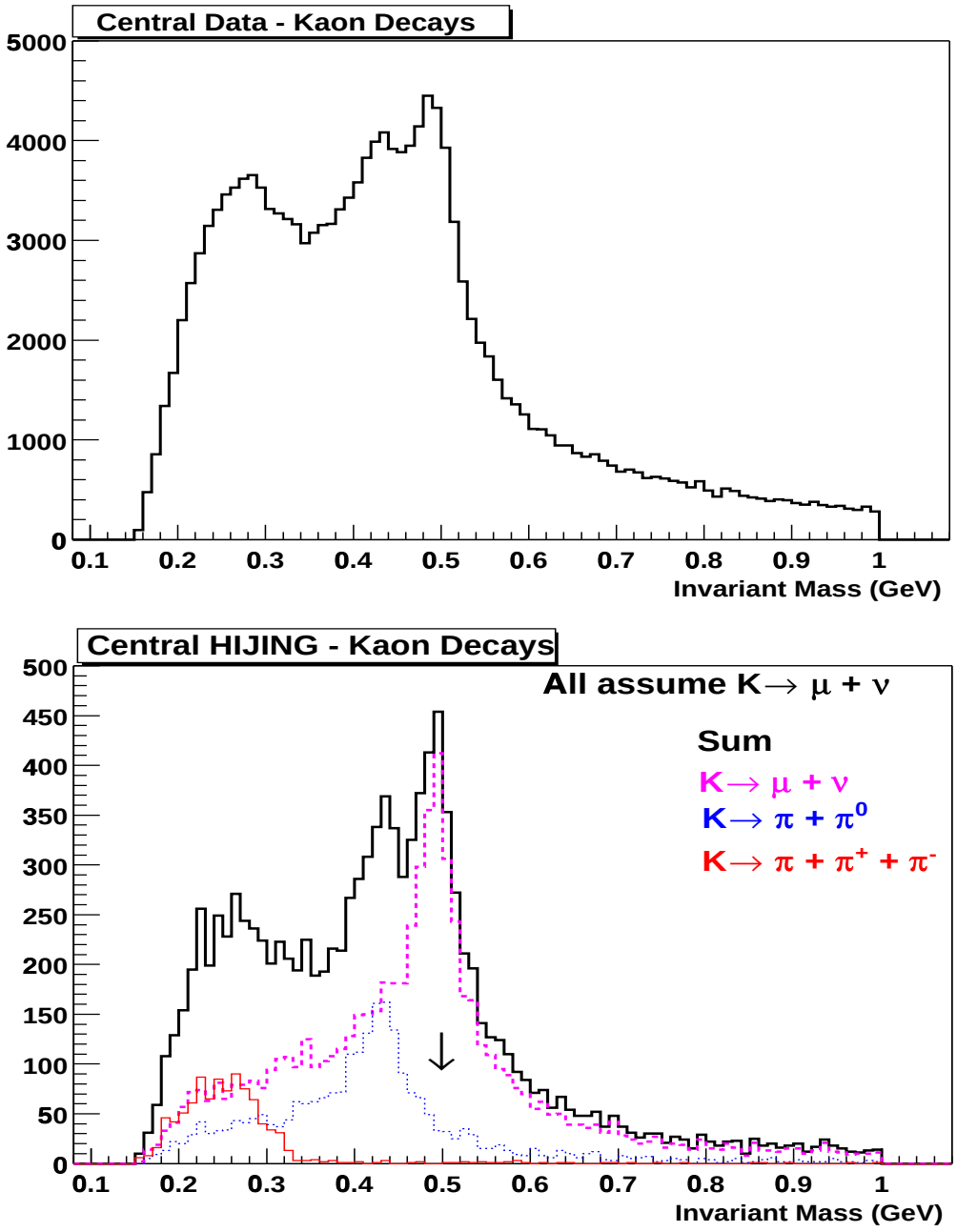

Figure 14: Kaon invariant mass assuming $K^{\pm} \rightarrow \mu^{\pm} + \nu$

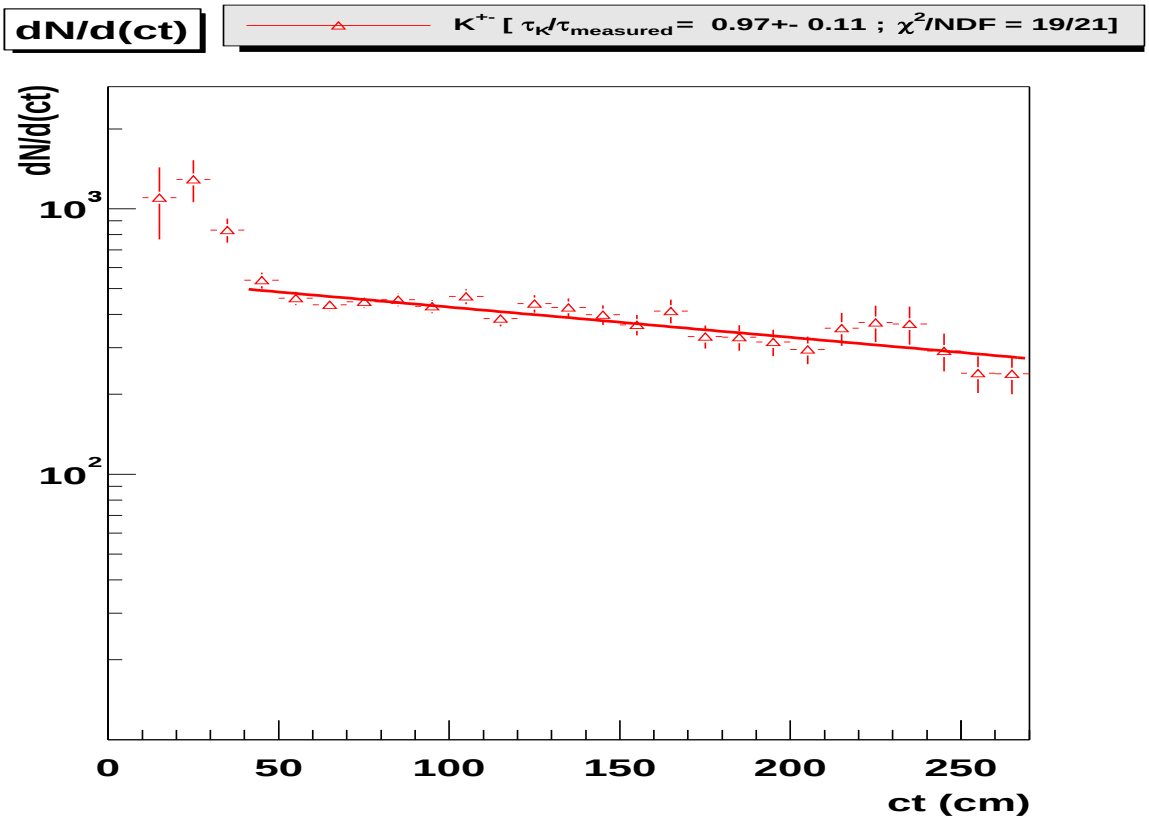

Figure 15: kaon life time

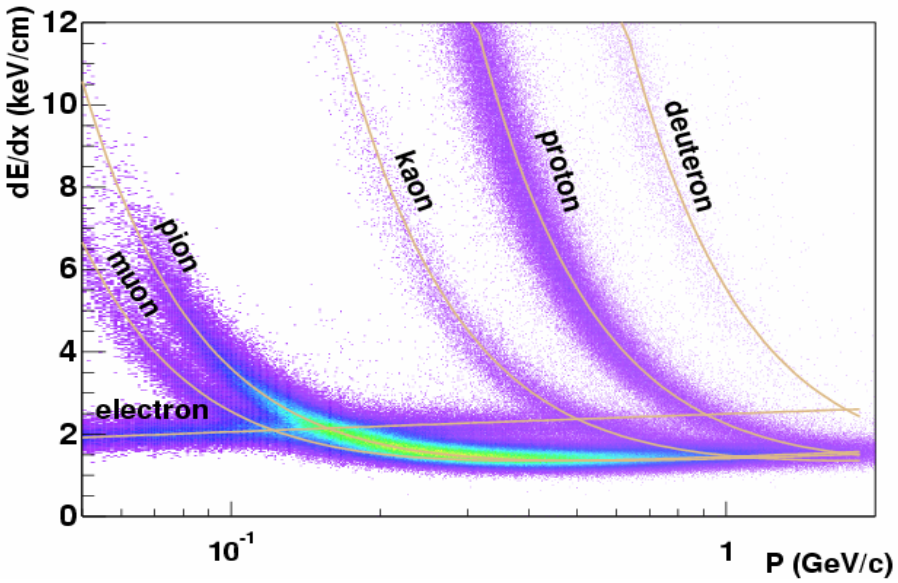

Figure 16: Mean dE/dx vs. momentum

CHAPTER 5

Results and Discussion

5.1 Event selection and Data Sample

We mentioned before that for this data set (first RHIC run in year-2000), the beam interaction zone (beam diamond) had an approximately Gaussian shape in both directions with an RMS of about 1mm in the transverse and 90 cm in the longitudinal direction. In order to avoid edge effects all events with a reconstructed vertex outside ± 60 cm from the TPC center were rejected. Another event selection criterion was the event multiplicity around mid-rapidity, but this was used to just characterize the centrality of the event.

The analyzed data sample is about half a million of central (ZDC triggered) events and half a million minimum bias events. About one hundred thousand kaons are included in the final physics plots, after all analysis plus event cuts are applied.

5.2 The K^+/K^- ratio

To give some background of statistical theory, we consider first the case $\mu_u = \mu_d = \mu_s = 0$ corresponding to a quark-gluon plasma with no net baryon content, as might be produced in the central rapidity region with heavy-ion collisions at very high energies. In this case, when $\mu_u = \mu_d = \mu_s = 0$ and when the temperature T is of the same order as the strange quark mass m_s, the density of all quarks and antiquarks are nearly the same . In such a plasma, the content of strange quarks and strange antiquarks is much greater then what one would expect in an equilibrated hadron gas without a phase transition. Hence, an enhancement of the number of strange quarks and antiquarks is suggested as a signal for the presence of a quark-gluon plasma. The enhancement of the number of strange quarks

and antiquarks leads to an enhancement of the production of mesons with an s or an $\bar{s}$ as a constituent.

In the heavy-ion stopping regime where one hopes to produce a quark-gluon plasma with a large net baryon density, the baryons which participate in the collision contain valence u and d quarks. Because of the conservation of baryon number, the baryon content of the colliding nuclei gives rise to the resultant baryon-rich quark matter, with nonzero quark chemical potentials μ_u and μ_d. On the other hand, with no valence strange quarks in the colliding nuclei the strange quark chemical potential μ_s is zero and the densities of s and $\bar{s}$ are the same.

At a temperature of T=0, the results of calculation give $\mu_u = \mu_d = 434$ MeV as the value of the up quark and the down quark phase transition chemical potential , above which the transition from the hadron phase to the quark-gluon plasma phase occurs. As the temperature T increases, there is an additional contribution to the pressure, one expects therefore that the value of the phase transition chemical potential μ_u or μ_d decreases. Since the quark matter created in the heavy-ion reactions in the stopping regime has a temperature of the order of a hundred MeV, the phase transition chemical potential μ_u or μ_d should be lower than the value of $\mu_{u,d} = 434$ MeV at T=0. In this case with nonzero chemical potentials $\mu_{u,d}$, the densities of u and d are greater than the density of s and $\bar{s}$ which in turn are greater than the densities of $\bar{u}$ and $\bar{d}$.

Consider the fate of an s quark and an $\bar{s}$ antiquark in a medium with nonzero chemical potential $\mu_{u,d}$. Because the densities of u and d are greater than the densities of $\bar{u}$ and $\bar{d}$, it is much more likely for the $\bar{s}$ antiquark to combine with a u or a d quark to form $K^+(u\bar{s})$ or $K^0(d\bar{s})$ than it is for the strange quark s to combine with a $\bar{u}$ or a $\bar{d}$ to form $K^-(\bar{u}s)$ or $\bar{K}^0(\bar{d}s)$. For the strange quark s, a more likely outcome is for it to combine with u and d quarks to form $\Lambda(uds)$, $\Sigma^+(uus)$, $\Sigma^0(uds)$, or $\Sigma^-(dds)$, instead of combining with $\bar{u}$ and $\bar{d}$ to produce $\bar{K}^0$ and K^-. Experimental measurements which can probe the numbers of s

and $\bar{s}$ relative to the numbers of u, d, $\bar{u}$ and $\bar{d}$ can be used to find out the thermodynamical state of the quark-gluon plasma in the stopping region.

It was shown [53, 54, 55] that ratios provide an excellent method for determining the temperature and the chemical potential since many theoretical and experimental uncertainties cancel out. Particle ratio is an important tool for investigating the mechanisms of particle production and the dynamics of collision systems.

5.2.1 Ratio of K^+/K^- vs. p_T

Figure 1 shows the distribution of K^+/K^- vs. p_T in the range $0.2 < p_T < 0.6$ GeV/c for the 11% most central collisions within $|y| < 0.5$ at mid-rapidity. By 11% we mean the most central part of the total inelastic cross section of Au+Au, assumed to be around 7.2 barn. The determination of the fraction of the percentages was done in a different study [44].

The ratio number found by fitting to a constant is $1.14 \pm 0.013(stat.)$. The same ratio measured by the dE/dx method is $1.083 \pm 0.008(stat.)$. The systematic errors are estimated to be 0.05 for kink and 0.03 dE/dx. Those two measurements are in good agreement within the quoted errors. In Figure 2 we extend p_T to 2 GeV/c, the K^+/K^- ratio reported by the kink method is $1.14 \pm 0.009(stat.)$ and shows no significant deviation from a constant value as a function of p_T.

In STAR we also have the ratio measurements of $\bar{\Lambda}/\Lambda$ and $\bar{p}/p$. The $\bar{\Lambda}/\Lambda$ ratio is $0.69 \pm 0.01(stat.)$. The $\bar{p}/p$ ratio is $0.65 \pm 0.01(stat.)$. Those data can explained by the quark coalescence model [45], which predicts the interesting relations for the antiparticle-particle ratios:

$$\frac{\bar{\Lambda}}{\Lambda} = \frac{K^+}{K^-} \cdot \frac{\bar{p}}{p}, \tag{5.1}$$

By using the measured Lambda and proton ratios one can "predict" the kaon ratio, if the model's assumption works. The predicted value is in excellent agreement with our direct measurements.

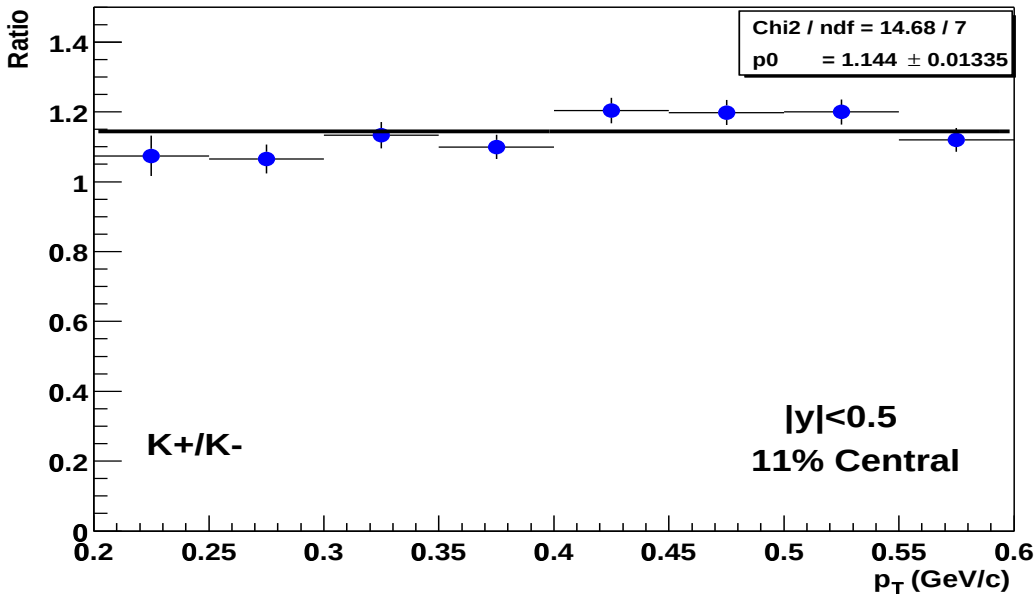

Figure 1: The K^+/K^- ratio vs. p_T at lower p_T

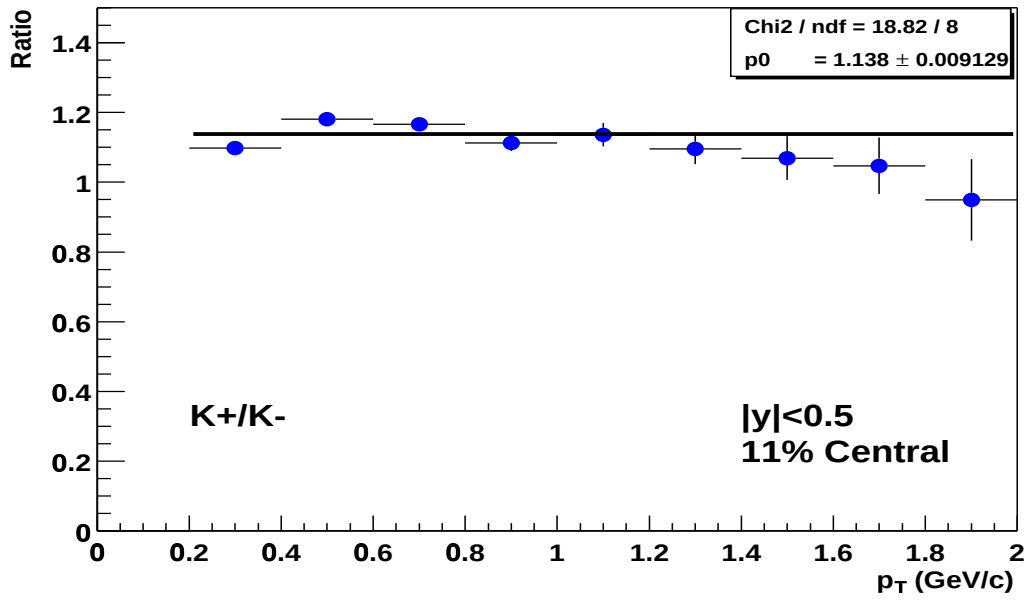

Figure 2: The K^+/K^- ratio vs. p_T

The measured kaon ratio is very close to one which signals a rather net-baryon free midrapidity region. In an opposite scenario, i.e. baryon rich environment, relevant at lower energies, the ratio takes much larger values due to the present of valence quarks from the participating nucleons. Let us try to quantify a bit more these results within the framework of a thermal model. Much effort has been devoted to the analysis of particle production within the framework of statistical models. These approaches are applied to the results of both elementary collisions and heavy ion collisions. The application of a statistical model usually requires that the measurement is done over the whole phase-space, i.e., with 4π particle yields. This is because conservation laws that apply to the collisions (like baryon number conservation or total net strangeness content zero) are only valid for global measurements, not locally. This procedure strongly reduces the possible influence of dynamical effects on particle yields and guarantees that the conservation laws of quantum numbers are fulfilled. In the restricted acceptance near midrapidity one needs to account for additional uncertainties in the derivation of thermal conditions from the experimental data. It is not excluded that thermal parameters at midrapidity could deviate from their values in full phase space as already seen at the SPS energy [56]. Fortunately, the current RHIC energy is sufficiently high, and such that data exhibit a boost-invariant rapidity plateau. Thus, the analysis near midrapidity should be little influenced by dynamical effects such as, e.g., hydrodynamical flow.

In Ref. [57], the authors present their analysis of particle ratios measured in Au+Au reactions at $\sqrt{s_{NN}} = 130$ GeV from the four RHIC experiments. The particle ratios are fitted with the statistical model. The best fit gives $T_{ch} \simeq 174 \pm 7$ MeV and $\mu_B \simeq 46 \pm 5$ MeV at this RHIC energy.

The fact that the substantial decrease of the baryon chemical potential from $\mu_B \simeq$ 270 MeV at SPS to $\mu_B \simeq 45$ MeV at RHIC suggests that we have created a low net baryon density state at mid-rapidity at RHIC where particle production mechanisms may

be dominated by gluon induced processes.

5.2.2 Ratio of K^+/K^- vs. rapidity

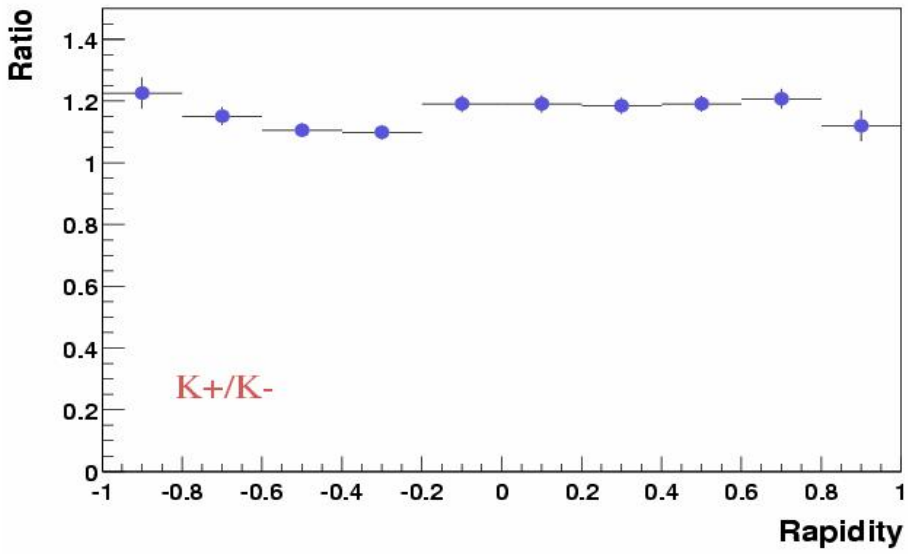

Figure 3: The K+/K- ratio versus rapidity.

The kaon ratio as a function of rapidity (in our limited rapidity acceptance around mid-rapidity) is shown in Fig. 3. The ratio is rather flat within $\mid y \mid < 1$, suggesting no dependence of ratio on rapidity in this very limited rapidity range. Since Au+Au is a symmetric system the ratio should be symmetric around mid-rapidity (modulo possible trigger biases which are very unlikely in our colliding environment). The relative scattering of points symmetric to mid-rapidity was used as one of the systematic error estimators.

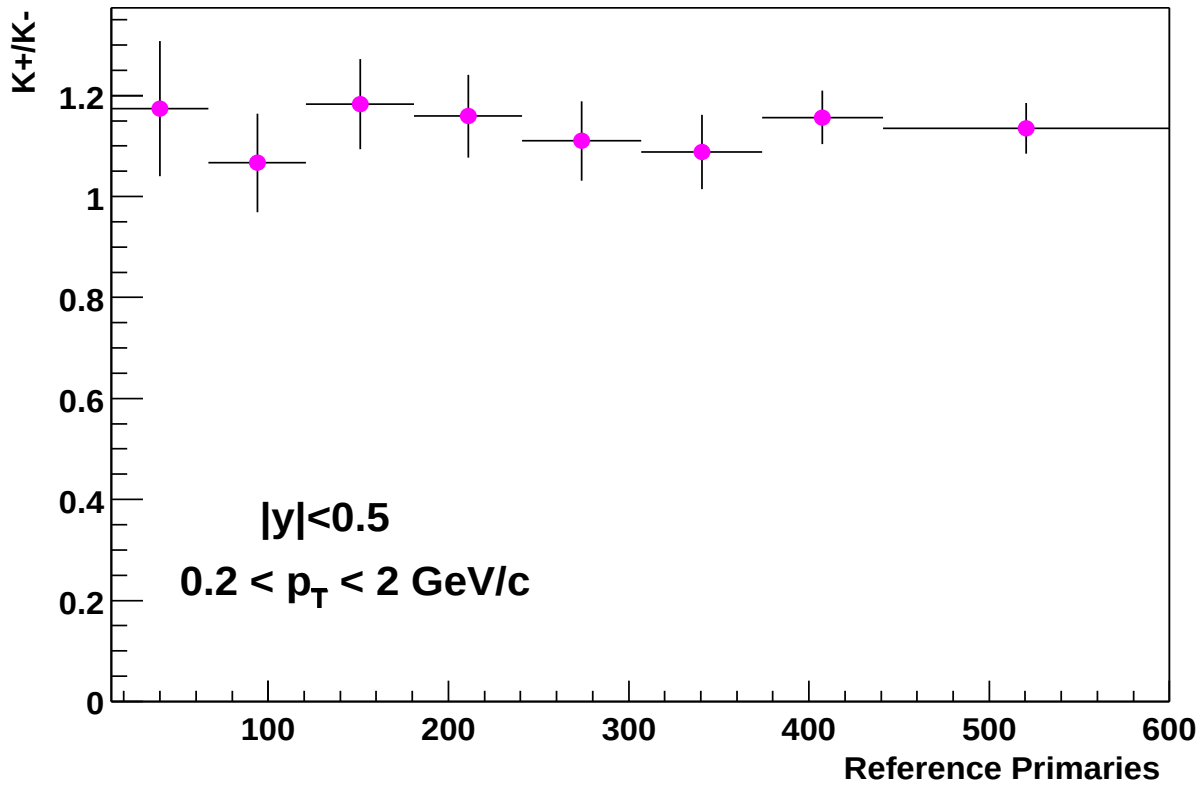

Figure 4: The K+/K- ratio versus centrality.

5.2.3 Ratio of K^+/K^- vs. centrality

Figure 4 shows the kaon ratio as a function of centrality. The horizontal axis in the figure is a measure of the total multiplicity of the event, therefore central events are on the right side of this figure. The ratio shows no apparent dependence to centrality. Maybe there is no significant change of physical mechanism from peripheral to central collisions albeit the differences in system overlap sizes. Another explanation might be that in central collisions there are more K^-'s with respect to K^+'s produced than in peripheral collisions. Combined with higher absorption of K^-'s in central collisions, it may make the net K^+/K^- ratio insensitive to collision centrality.

One has to note here that even at our most peripheral bin, a large part of the cross

section is left out, in other words, our most peripheral bin is still far from approximating the elementary nucleon-nucleon case.

5.3 Spectra of K^+ and K^-

Transverse momentum or mass distributions are one of the most common tools used in studying high energy collisions. This is because the transverse motion is generated during the collision and hence is sensitive to the dynamics, plus the fact that it is unaffected by Lorentz transformations.

Most particle multiplicities measured in nucleus-nucleus collisions are well consistent with thermal model predictions. If the system is in local thermal equilibrium, then the observed momentum or mass spectra should reflect the (average) temperature. However, since a thermalized source which is surrounded only by vacuum must necessarily begin to expand, the thermal motion is superimposed in the spectra by a dynamical component arising from the collective expansion. This is most clearly seen in the measured longitudinal momentum or rapidity spectra of hadrons from heavy ion collisions which for both Brookhaven and CERN energies are much broader than a thermal distribution from a stationary fireball; the strong collective flow component here is partially due to incomplete stopping of the colliding nuclei and partially due to additional hydrodynamical expansion generated in the later stages of the collision.

In the transverse direction, where the momentum spectra look approximately exponential like a thermal distribution, the identification of a collective flow component is more involved; one needs to perform a systematic study of the 'apparent' temperatures (slope parameters as a function of particle mass) in order to be able to extract transverse flow information. In a simple non-relativistic picture, if we assume the presence of collective transverse flow, i.e. transverse common velocity, particles of heavier mass will exhibit shifts to higher momenta and thus a higher inverse slope parameter; the spectra are 'blue shifted'. This effect was first observed in CERN-SPS data, where the slope parameter showed an almost linear increase with the particle mass. Once one obtains the various particle spectra a simultaneous fit can result in the flow velocity and the 'real' as opposed to 'apparent'

temperature.

The strange particles are good indicators for collective flow, because all are produced particles which were absent in the original nuclei and are thus not contaminated by a cold spectator component at leading rapidities as the protons are. Also because of their bigger mass their flow component is more accentuated against the random thermal motion as in the case of the pions.

5.3.1 Transverse momentum (p_T) and mass (m_T) distribution

Figure 5 and 6 show transverse momentum distributions d^2N/dp_Tdy versus p_T for K^+ and K^- at different centralities. This and all subsequent spectra are background subtracted and acceptance and efficiency corrected. Note that those are the linear dN/dp$_T$ plots, in other words the actual measurement before any manipulation, i.e. division by 1/p$_T$, log scale etc. They usually serve to demonstrate in a direct way the quality of the measurement and also the quality of the performed fits.

The fit function we use has the general Boltzmann-inspired form of

$$\frac{d^2N}{dp_Tdy} = A \cdot p_T \cdot e^{-\sqrt{m_K^2+p_T^2}/T} \tag{5.2}$$

where m_K is the kaon rest mass, A and T are fit parameters. A can be related the yield dN/dy and T is the inverse slope parameter. The fit qualities are shown in table 2.We observe that the fit quality slightly degrades as we go from central to peripheral data. To compare to other experiments, we will use the fit parameters derived from transverse mass spectra.

Figure 7 and 8 shows the transverse mass spectra of the invariant yields of K^+ and K^- from the kink calculation, Figure 9 the comparison plots with the dE/dx and K^0_S, respectively. Here, the transverse mass is $m_T = \sqrt{p_T^2 + m_K^2}$, and m_K is the kaon rest mass. Given that the three analyzes are vastly different, the agreement is remarkable.

The spectra exhibit an exponential shape in m_T. We fit the spectra to a m_T exponential

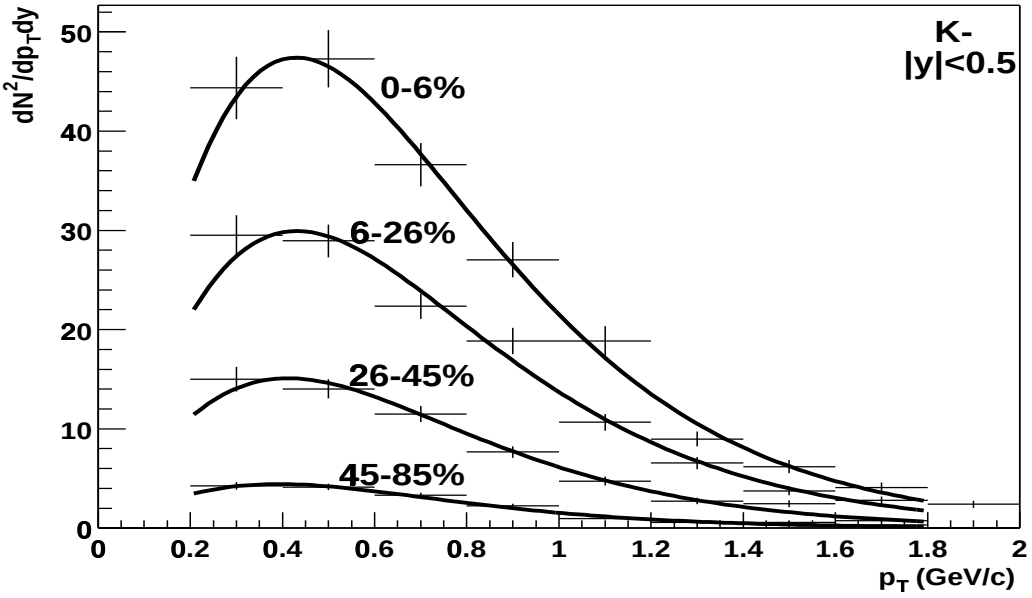

Figure 5: The K- transverse momentum distribution

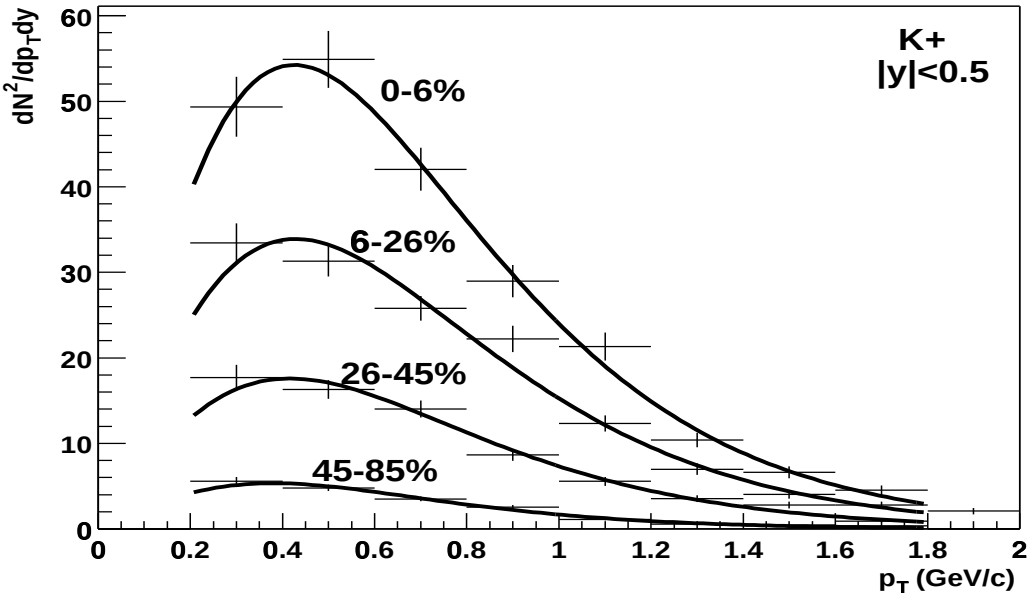

Figure 6: The K+ transverse momentum distribution

with the inverse slope T and the integrated rapidity density dN/dy treated as two free parameters. The fit results are listed in Table 1 for each centrality bin, together with $dN_{h^-}/d\eta$, the average pseudo-rapidity density of negative hadrons [46].

Centr. bin	$\frac{dN_{h^-}}{d\eta}$	$\frac{dN_{\pi^-}}{dy}$	K^+(dEdx) dN/dy	K^+(dEdx) T	K^-(dEdx) dN/dy	K^-(dEdx) T	K^+(Kink) dN/dy	K^+(Kink) T	K^-(Kink) dN/dy	K^-(Kink) T	K^0_S dN/dy	K^0_S T
58-85%	17.9	18.2	2.5±0.1	238±18	2.4±0.1	235±19						
45-58%	47.3	48.0	7.2±0.5	248±19	6.3±0.4	257±20	3.9±0.2	238±8	3.5±0.2	246±9	3.27±0.04	267±2
34-45%	78.9	79.1	13.6±0.9	299±22	11.3±0.7	266±19						
26-34%	115	116	19.3±1.6	322±27	15.2±0.9	264±19	15.2±0.5	267±8	12.9±0.5	262±8	12.0±0.1	279±2
18-26%	154	151	24.3±1.8	296±24	23.5±1.9	317±26						
11-18%	196	192	31.9±2.2	301±23	29.2±2.3	306±25	30.1±0.9	277±7	26.9±0.8	283±7	25.2±0.2	288±2
6-11%	236	232	37.9±2.1	297±17	35.1±2.1	296±18						
0-6%	290	285	45.5±2.2	282±15	43.3±2.3	296±16	47.8±1.5	279±6	42.1±1.3	283±6	39.6±0.6	289±3

Table 1: Comparison among the kaons from dE/dx, Kink and K0

Centrality bin	χ^2/ndf K^+	χ^2/ndf K^-
0-6%	0.87	1.17
6-26%	1.53	1.17
26-45%	1.40	1.25
45-85%	2.35	2.44

Table 2: The fit qualities of p_T spectra

5.3.2 The inverse slope systematics

Figure 10(a) shows the kaon inverse slope T as a function of $dN_{h^-}/d\eta$. No difference is observed between K^+ and K^-. For the top 6% central events the inverse slopes are 279 ± 6 MeV and 283 ± 6 MeV for K^+ and K^- respectively. There is an indication that the inverse slope increases with $dN_{h^-}/d\eta$, from ~ 240 MeV for the most peripheral bin to ~ 280 MeV for the most central bin. STAR also measures the inverse slope of negative pions which is 190 ± 15 MeV, and that of anti-proton, 374 ± 9 MeV for the most central bin. There is an indication of a mass dependence of the inverse slopes. In a hydrodynamic picture, matter flows, i.e., particles of different mass all move with the same velocity. Classically, the collective kinetic energy will then depend on the particle mass: Particles with higher mass

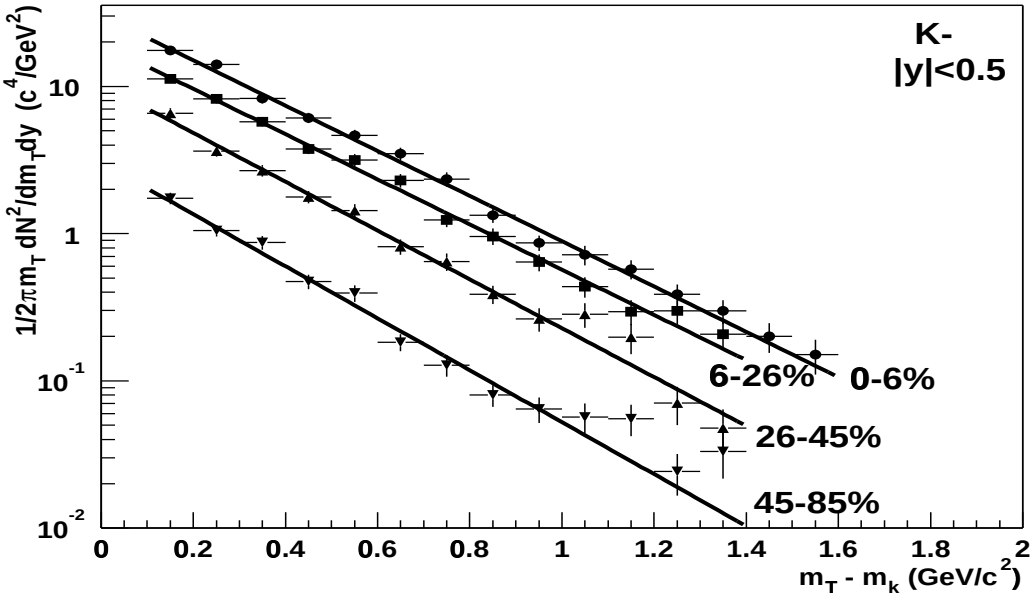

Figure 7: The K- transverse mass distribution

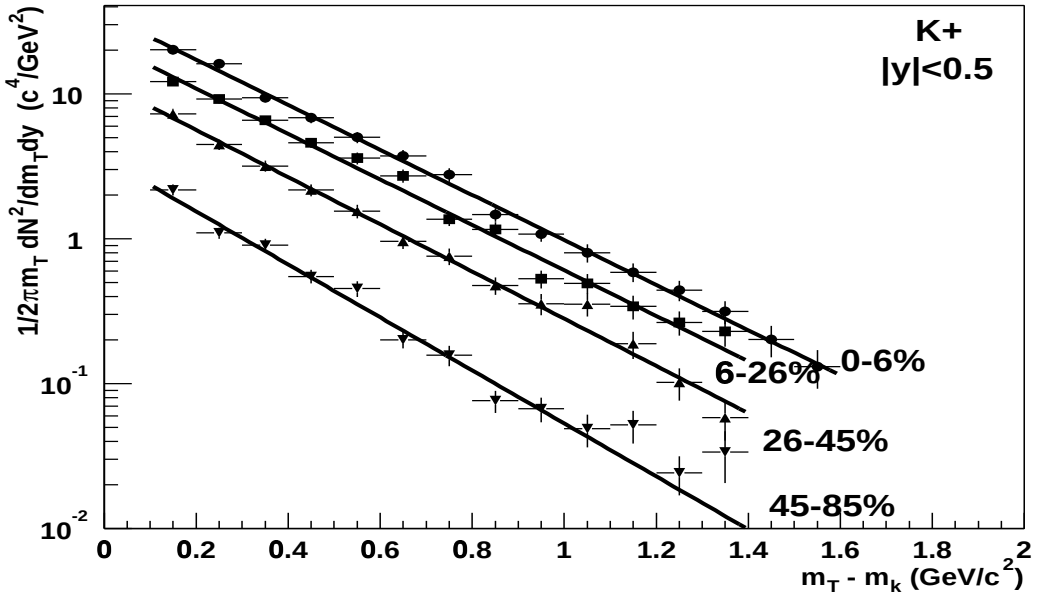

Figure 8: The K+ transverse mass distribution

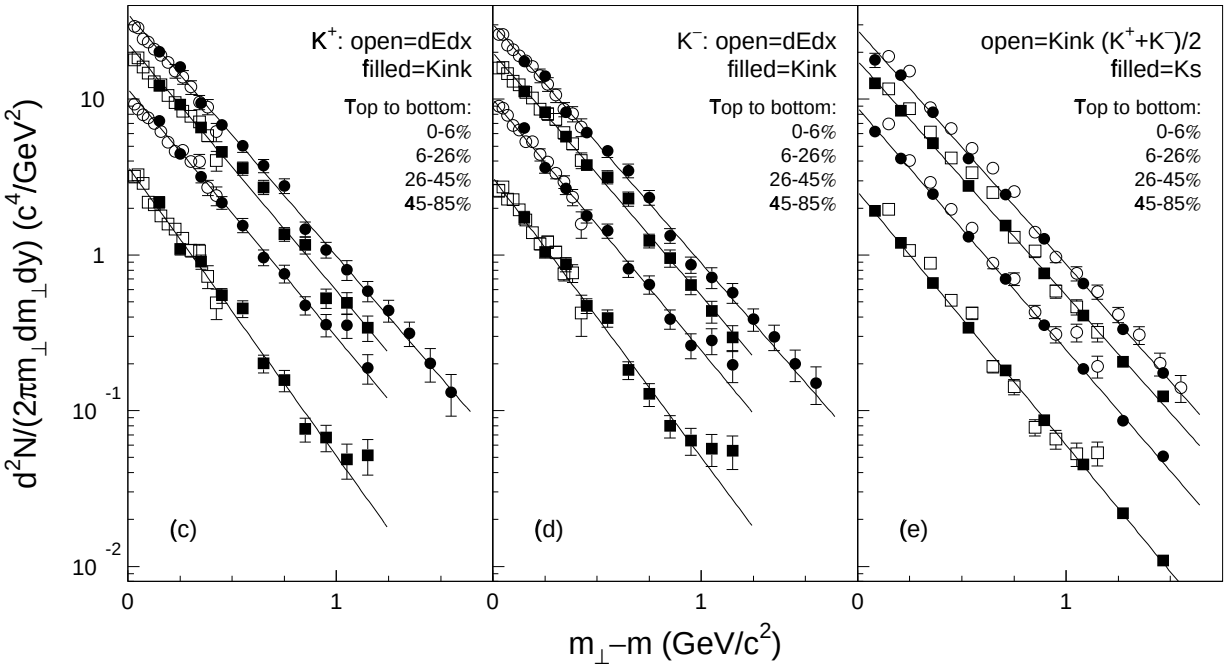

Figure 9: Kaon invariant yield m_T spectra

will carry more momentum. The experimental slope parameter measures the particle energy which contains both thermal (random) and collective (due to secondary collisions among the produced particles, or rescattering) contributions. The intrinsic freeze-out temperature, namely, the temperature when the particles cease to interact with each other, is determined by the thermal motion. As rescattering is not important in p + p collisions, the slope parameter should be due only to the thermal motion and thus may reflect the true freeze-out temperature. This interpretation is strengthened by the observation that the slope parameter remains nearly constant (around 140-150 MeV) for all particles from the p + p data. When the size of the colliding nuclei increases, so does the number of rescatterings and, as a consequence, collective motion develops. By performing a simultaneous fit of all available particle species [47], the resulting flow velocity is $\beta = 0.5 - 0.6c$ with a freezout temperature of $T = 140\,\mathrm{MeV}$. Comparing to the SPS data where $\beta \approx 0.4c$, the slope parameter systematic of pion, kaon and proton shows an stronger dependence on the particle

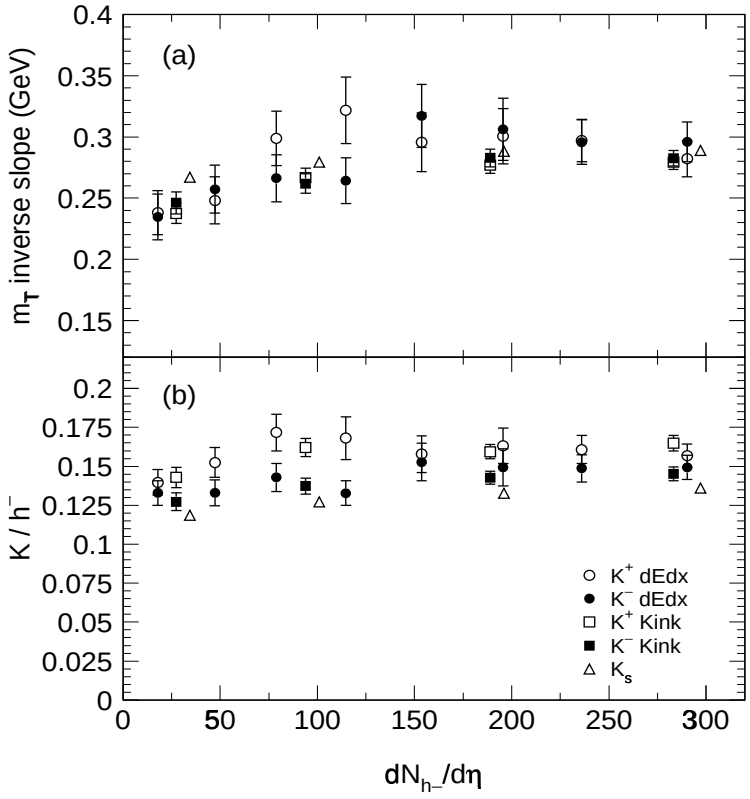

Figure 10: Centrality dependence of: (a) kaon inverse slopes and (b) mid-rapidity kaon to negative hadron ratios.

mass at RHIC energy. The strong energy dependence of the slope parameter might be the result of the larger pressure gradient indicating a violent, explosive expansion of the fireball at RHIC energies.

5.3.3 The rapidity density and the K/π ratio

The measured particle yields at mid-rapidity are 47.8 ± 1.5 and 42.1 ± 1.3 for K^+ and K^- respectively, for the top 6% central events. Figure 10(b) shows the kaon dN/dy to $dN_{h^-}/d\eta$ ratio as a function of $dN_{h^-}/d\eta$. No strong centrality dependence is observed for the ratio,

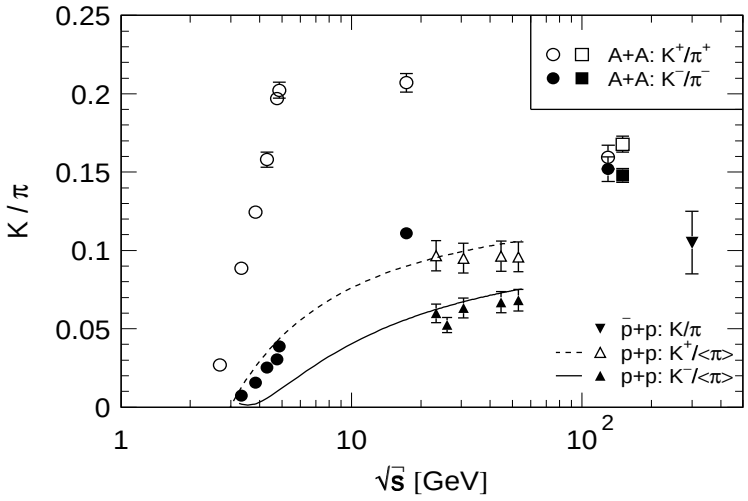

Figure 11: Mid-rapidity K/π ratios versus $\sqrt{s_{NN}}$. The kink results (squares) are displaced in $\sqrt{s_{NN}}$ for clarity.

suggesting no significant change in strangeness production mechanisms from peripheral to central collisions.

In order to evaluate K/π, we deduce the pion dN_{π^-}/dy from our measurements of $dN_{h^-}/d\eta$ by using our results on kaon and antiproton production. The estimated yields are reported in Table 1. The deduced dN_{π^-}/dy is consistent with our preliminary measurement of pion spectra. The K/π ratios are similar to the ratios of kaon dN/dy to $dN_{h^-}/d\eta$ shown in Figure 10(b). The values for the most central events are $K^+/\pi^+ = 0.16 \pm 0.01 \pm 0.02$ and $K^-/\pi^- = 0.15 \pm 0.01 \pm 0.02$. The K/π ratio has been intensively studied at low

energies. Figure 11 compiles K/π results for central heavy ion collisions. As no difference is observed between π^+ and π^- mid-rapidity multiplicities at RHIC, we can readily compare our K^+/π^- result to K^+/π^+ at low energies. The K^-/π^- ratio steadily increases with $\sqrt{s_{NN}}$, while the K^+/π^+ ratio in heavy ion collisions sharply increases at low energies. The addition of our K^+/π^+ measurement clearly demonstrates that K^+/π^+ drops at high energies. The maximum value of K^+/π^+ seems to be reached in the $\sqrt{s_{NN}}$=10 GeV energy region. The reason for this behavior of K^+/π^+ may lie in the net-baryon density which changes significantly with $\sqrt{s_{NN}}$, as noted previously [48, 49]. It is instructive to consider the two possible kaon production mechanisms: pair production of K and $\overline{K}$ (sensitive to collision energy) and associated production of K with a hyperon and $\overline{K}$ with an antihyperon (sensitive to net-baryon density). The relative contribution of associated to pair production can be more clearly demonstrated by the K^+/K^- ratio, which is a monotonically decreasing function of $\sqrt{s_{NN}}$. In other words, a maximum in K^+/π^+ results from a dropping net-baryon density with energy and an increasing production rate.

Figure 11 also shows for comparison parameterizations to p+p data (curves) and data from p+p ([50]) and $\bar{p}$+p ([51]) at high energies. Our measurement indicates a 50% enhancement over p+p and $\bar{p}$+p collisions at similar energies. The enhancement in K^-/π is similar at SPS and RHIC, while that in K^+/π is larger at lower energies due to effects of net-baryon density.

5.4 Summary

Using a method for a topological identification of charged kaon decays, we have measured the charged kaon ratio, spectra and rapidity densities at mid-rapidity.

The K^+/K^- ratio is close to unity which is an indicator of an almost net-baryon free mid-rapidity region. The measured ratio is compatible with other strange and non-strange particle ratios in the same experiment in a simple quark coalescence model, all of them

indication a near net-baryon free environment at RHIC mid-rapidity.

The charged kaon spectra exhibit high inverse slope parameters ($T = 290\,\mathrm{MeV}$). This together with measurements of slope parameters of other particle species resulted in a strong indication of explosive transverse flow at RHIC energies. Flow velocities of $\beta = 0.5 - 0.6c$ and freezout temperatures of 140 MeV where found after performing hydrodynamical fits to all available STAR data. Large flow is an indicator of the presence of high pressure in the system early in its evolution. Particle rescattering (thermalization?) could be the intuitive driving factor of this effect.

The rapidity densities of charged kaons are directly related to the question of strangeness enhancement since kaons carry 70-80% of the total number of produced strange quarks. The measured densities show an enhanced production of strangeness at RHIC relative to elementary nucleon-nucleon system as indicated by the systematics of the K/π ratio. The magnitude of the enhancement is similar to that observed at the CERN SPS program. One has to notice thought that unlike at SPS the pion production at RHIC has also been found to be enhanced relative to nucleon-nucleon system; for the first time the entropy production is not linearly proportional to the number of participating nucleons.

The K/pion systematics also show that the dominant kaon production mechanism at RHIC is direct pair production, in contrast to lower energies where 'associated production'–like mechanisms dominate.

These results are very encouraging since they demonstrate that the RHIC environment is quite different from what physicists were used to up to now. Also the first results indicate a behavior which departs from nucleon-nucleon collisions, a strong evidence of collective (nuclear) phenomena. As the initial, 'global' mapping of the collisions comes to a conclusion more penetrating (hard) probes are needed so that definite statements can be made on the QGP creation questions.

BIBLIOGRAPHY

[1] Stachel J, Young GR. *Annu. Rev. Nucl. Part. Sci.* 42:537 (1992)

[2] Harris JW, Müller B. *Annu. Rev. Nucl. Part. Sci.* 46:71 (1996)

[3] Heinz U, Jacob B. nucl-th/0002042 (2000)

[4] Riccati L, Masera M, Vercellin E, eds. *Proc. of 14th Int. Conf. on Ultra-Relativistic Nucleus-Nucleus Collisions, Quark Matter '99, Torino, Italy. Nucl. Phys* A661 (1999)

[5] Carruthers P, Rafelski J, eds. *Proc. Hadronic Matter in Collision, Tucson, AZ, 1988.* Singapore, World Scientific (1989)

[6] Vassiliadis G, Panagiotou AD, eds. *Proc. Int. Symposium on Strangeness and Quark Matter, Crete, Greece, 1994.* Singapore: Word Scientific (1995)

[7] Rafelski J, ed. *Proc. Strangeness in Hadronic Matter, Tucson, AZ, 1995. Am. Inst. of Physics Conf. Procs.* 340 (1995)

[8] Csörgő T, Lévai P, and Zimányi J, eds. *Proc. Conf. on Strangeness in Quark Matter, Budapest, Hungary, 1996. Acta Physica Hungarica N.S. Heavy Ion Physics* 4 (1996)

[9] Panagiotou AD, ed. *Proc. Int. Symposium on Strangeness in Quark Matter, Santorini, Greece, 1997. J. Phys. G* 23(12) (1997)

[10] Morando M, ed. *Proc. Int. Symposium on Strangeness in Quark Matter, Padua, Italy, 1998. J. Phys. G* 25(2) (1999)

[11] Rafelski J, Hagedorn R. *Proc. Int. Symposium on Statistical Machanics of Quarks and Hadrons, Bielefeld*, p. 253. Amsterdam: North-Holland (1981)

[12] Rafelski J. *Phys. Rep.* 88:331 (1982)

[13] Rafelski J, Müller B. *Phys. Rev. Lett.* 48:1066 (1982). Erratum. *Phys. Rev. Lett.* 56:2334 (1986)

[14] Rafelski J. *Nucl. Phys.* A418:215 (1984)

[15] Gottfried K, Weisskopf VF. *Concepts of Particle Physics*, Vol. 2, p. 397. New York: Oxford University Press (1986)

[16] Müller B. *Rep. Prog. Phys.* 58(6):611 (1995)

[17] Wróblewski A. *Acta Physica Polonica* B16:379 (1985)

[18] Matsui T, Svetitsky B, McLerran LD. *Phys. Rev. D* 34:783 (1986). Erratum. *Phys. Rev. D* 37:844 (1988)

[19] Koch P, Müller B, Rafelski J. *Phys. Rep.* 142:167 (1986)

[20] Heinz U. *Nucl. Phys.* A566:205 (1994)

[21] Rafelski J. *Phys. Lett.* B262:333 (1991)

[22] Sollfrank J. *J. Phys. G* 23:1903 (1997)

[23] Becattini F. *Z. Phys. C* 27:485 (1996)

[24] Becattini F, Heinz U. *Z. Phys. C* 76:269 (1997)

[25] Sorge H, Berenguer M, Stöcker H, Greiner W. *Phys. Lett.* 289B:6 (1992)

[26] Aichelin J, Werner K. *Phys. Lett.* 300B:158 (1993)

[27] Capella A, Ferreiro EG, Salgado CA. *Phys. Lett.* 459B:27 (1999)

[28] Andersson B, et al. *Nucl. Phys.* B281:289 (1987)

[29] Nilson-Almquist B, Stenlund E. *Comp. Phys. Comm.* 43:387 (1987)

[30] Werner K. *Z. Phys. C* 38:193c (1988)

[31] Sorge H, Stöcker H, Greiner W. *Nucl. Phys.* A498:567c (1989)

[32] Bass SA, et al. *Proc. Int. Conf. Nucl. Phys. at Turn of Millennium, Wilderness, South Africa, March 1996*, p. 399. Singapore: World Sci. (1997)

[33] Bass SA, et al. *Prog. Part. Nucl. Phys.* 41:225 (1998)

[34] Pang Y, Schlagel TJ, Kahana SH. *Phys. Rev. Lett.* 68:2743 (1992)

[35] Antinori F. et al. See Ref. [10] p. 345

[36] Antinori F. et al. *Eur. Phys. J.* C11:79 (1999)

[37] Müller B. See Ref. [4], p. 272c

[38] Geiger K. *Comp. Phys. Comm.* 104:70 (1997). nucl-th/9806102 (1998)

[39] Wang XN, Gyulassy M. *Phys. Rev. D* 44:3501 (1991)

[40] Wang XN, Gyulassy M. *Phys. Rev. D* 45:844 (1992)

[41] Wang XN, Gyulassy M. *Comp. Phys. Comm.* 83:307 (1994)

[42] Bass SA, et al. *Phys. Rev. C* 60:021901 (1999)

[43] STAR coll., H. Wieman et al. *Nucl. Phys.* A661:681 (1999)

[44] M. Calderon *Ph.D. Thesis* Yale University (2001)

[45] J. Zimányi, T. S. Biró, T. Csörgő, P. Lévai, *hep-ph*/9904501

[46] C. Adler *et al.* (STAR Collab.), Phys. Rev. Lett. **87**, 112303 (2001).

[47] Nu Xu and Masashi Kaneta, *arXiv:nucl-ex*/0104021

[48] F. Wang, *Phys. Lett.* B 489, 273 (2000).

[49] F. Wang, H. Liu, H. Sorge, N. Xu and J. Yang, *Phys. Rev.* C 61, 064904 (2000); F. Wang and N. Xu, *Phys. Rev.* C 61, 021904 (2000); J.C.Dunlop and C.A.Ogilvie, *Phys. Rev.* C 61, 031901 (2000); P. Braun-Munzinger *et al.*, *hep-ph*/0106066.

[50] A.M. Rossi *et al.*, *Nucl. Phys.* B 84, 269 (1975); J.L.Baily *et al.* (NA27 Collab.), *Phys. Lett.* B 195, 609 (1987)

[51] T. Alexopoulos, *Phys. Rev.* D 48, 984 (1993).

[52] R. Brun, R. Hagelberg, M. Hansroul, and J. C. Lassalle, Technical Report No. CERN-DD-78-2-REV, CERN (unpublished).

[53] P. Braun-Munzinger, J. Stachel, J. Wessels, and N. Xu, Phys. Lett. B344, 43(1995); P. Braun-Munzinger, I. Heppe, and J. Stachel, Phys. Lett. B465, 15(1999).

[54] F. Becattini, M. Gazdzicki, and J. Sollfrank, Eur. Phys. J. C5, 143(1998); F. Becattini, Z. Phys. C69, 485(1996); F. Becattini and U. Heinz, Z. Phys. C76, 269(1997).

[55] J. Cleymans and K. Redlich, Phys. Rev. Lett. 81, 5284(1998).

[56] F. Becattini, J. Cleymans, A. Keranen, E. Suhonen, K. Redlich, hep-ph/0002267, Phys. Rev. C, in press.

[57] P. Braun-Munzinger, D. Magestro, K. Redlich, and J. Stachel, Phys. lett. B518, 41(2001)

APPENDIX A

.

Definition of Kinematic Variables

In relativistic high energy heavy ion collisions, It is convenient to use kinematic variables that are Lorentz invariant or transform trivially under Lorentz boost.

Given the z axis as the direction of the beam, the p_t (transverse momentum) is defined as:

$$p_t = \sqrt{p_x + p_y} \tag{A.1}$$

p_t is a Lorentz invariant variable since both p_x and p_y are unchanged under a Lorentz boost along z axis.

For identified particles one usually employs the transverse mass

$$m_t = \sqrt{{p_t}^2 + m^2} \tag{A.2}$$

where m is the mass of the particle. The transverse energy of the particle is given by $m_t - m$.

For the longitudinal momenta, it is normally to use the rapidity defined as

$$y = \frac{1}{2} \ln \left(\frac{E + p_z}{E - p_z} \right) \tag{A.3}$$

$$= \ln \left(\frac{E + p_z}{m_t} \right) \tag{A.4}$$

$$= \tanh^{-1} \left(\frac{p_z}{E} \right) \tag{A.5}$$

where E and p_z are the energy and longitudinal momentum of the particle.

Under a Lorentz transformation from a reference system S to a system S' moving with velocity β_z with respect to S in the longitudinal direction, the rapidity y' in the S' frame

is related to y in the S frame only by an additive constant: $y' = y - y_\beta$, where y_β is the rapidity of the moving frame.

(A.6) $$y_\beta = \frac{1}{2} \ln \left(\frac{1+\beta_z}{1-\beta_z} \right)$$

The additive of rapidity guarantees that the shape of the corresponding distribution is unchanged under Lorentz boost.

In the limit of $p \gg m$ and $p_z/p \gg 1/\gamma$, the rapidity comes to be

(A.7) $$y = \frac{1}{2} \ln \left(\frac{E+p_z}{E-p_z} \right) \approx \frac{1}{2} \ln \left(\frac{|\vec{p}|+p_z}{|\vec{p}|-p_z} \right) = \ln \left(\sqrt{\frac{1+\cos\theta}{1-\cos\theta}} \right) = -\ln(\tan\theta/2) \equiv \eta$$

where η is called pseudo-rapidity.